PSFC/JA-05-50

Theoretical and Experimental Contributions of MIT to the Fusion Science Center, and Findings of the Electron Transport Task Force

R. D. Petrasso, C. K. Li, F. H. Séguin, C. Chen and D. Casey

23 December 2005

Plasma Science and Fusion Center
Massachusetts Institute of Technology
Cambridge, MA 02139 USA

This work was supported in part by U.S. Department of Energy Contract #DE-FG03-99SF21782, LLE subcontract #PO410025G, LLNL subcontract #B313975, and the Fusion Science Center for Extreme States of Matter and Fast Ignition Physics at University of Rochester.

MIT PSFC Document PSFC/JA-05-50

Theoretical and Experimental Contributions of MIT to the Fusion Science Center, and Findings of the Electron Transport Task Force

R. D. Petrasso, C. K. Li, F. H. Séguin, C. Chen, D. Casey

Plasma Science and Fusion Center
Massachusetts Institute of Technology
Cambridge, MA 02139

Work in support of

University of Rochester Fusion Science Center for Extreme States of Matter

MIT Principal Investigators:
Richard. D. Petrasso and Chikang Li

27 December 2005

EXECUTIVE SUMMARY AND OVERVIEW

This report focuses on the work of the MIT group as it relates to the Fusion Science Center, and to the work MIT has led and coordinated with respect to Electron Transport Task Force (ETTF). We summarize herein the scope and context of the work, the essential findings and conclusions, and proposed theoretical and experimental work for the next 3 years.

Among the many important and complex processes involved in Fast Ignition (FI) are the assembly of a high-density (~ 300g/cc) DT plasma and then the rapid deposition of energy (from directed electrons or possibly protons), which ignites the assembled fuel. Though there are many complicated features of this problem, some of which are being addressed by other institutions and task forces within the FSC, MIT has focused on certain specific and important issues within this purview. The first concerns electron energy deposition in a DT plasma whose density is sufficiently high (~ 10^{24} to 10^{26} cm^{-3}) that interactions can be viewed as solely between the energetic "test" electrons and a dense background sea of electrons and D/T ions. Self fields and Weibel-like instabilities, processes crucial in electron beam formation and initial penetration, play a negligible role in such circumstances.

Important to proper treatment of the energy deposition in such dense plasmas, and to establishing quantitative FI threshold criteria, is the inclusion of both electron straggling and blooming, direct consequences of electron scattering off both background ions and electrons. For example, 1-MeV electrons penetrate on average 0.41 g/cm^2 in a 300 g/cc plasma, with blooming of ± 0.15 g/cm^2 , and straggling of ±0.09 g/cm^2 (0.41 g/cm^2 corresponds to 13.7 μm). In stark contrast to such electron scattering effects, protons that penetrate exactly as far as the 1 MeV electrons in this dense DT plasma (the proton energy would be 18.8 MeV) have blooming and straggling effects two orders of magnitude smaller than those of the electrons.

Such calculations, and many more to be discussed herein, were obtained by application of an electron stopping model developed in work that was led by Dr. C. K. Li. Fundamental to this model is the inextricable coupling between electron scattering and electron energy loss. Because this coupling is so essential to the calculations, we refer to the stopping model as the Coupled Energy Loss and Scattering Analysis, or CELSA, model (about which one paper has been published, two more have been accepted for publication, three are in preparation, and 7 presentations made at conferences, including an Invited talk at DPP/APS in 05.) To investigate the consequences of this model, we show herein many calculations that involve semi-realistic FI scenarios, such as energy deposition profiles of 1 MeV electrons injected into a uniform 300 g/cc DT plasmas; for this case, the radii of the electron beam footprint varies from near zero to 20 μm. From these results the combined effects of beam size and scattering, as manifest in blooming and straggling, can be clearly discerned.

A second issue of significance to FI and HEDP concerns the fuel assembly of the DT plasma and possible adverse effects that could arise from an increase in fuel adiabat due to excessive electron preheat; such could preclude proper fuel compression and assembly. As a first step in studying this preheat, we have applied the CELSA model to an examination of energy deposition of 20 to 200 keV electrons in a 10 eV DT plasma at the density of either solid DT ice (0.25 g/cc) or 4 times higher (1 g/cc). The results of CELSA calculations are contrasted to cold-matter Monte-Carlo calculations, and the effects of high-Z material on energy deposition, straggling and blooming are investigated, further illuminating the differences and similarities between cold matter and CELSA plasma calculations.

Related to both sets of problems, i.e. electron energy deposition and scattering in either dense or preheat plasma scenarios, is the question of whether definitive experimental tests of the CELSA model can or should be undertaken and, in particular, whether such tests could be

accomplished by performing an electron stopping experiment in cold matter. After careful consideration and many calculations (see, e.g., herein), and after extensive discussions with task force members (listed in Appendix A), we recommend that no such experiment be undertaken. The reasons are two: First, we are unable to definitively link any measurement in cold matter to unique and critical features of the CELSA model. While there are certainly similarities in both formulations, such as the profound effects of electron scattering, distinct and fundamental differences, such as plasma screening, make tests of veracity of one, that carry through unambiguously to the other, untenable and inconclusive. Second, given the vast literature and work on electron stopping in cold matter, we do not see how any plausible experiment MIT might lead in the next two years would advance, in a fundamental way, our existing base of knowledge of cold matter stopping for electrons. In addition, because of the extraordinary complexity of performing plasma stopping experiments for electrons, it too would be quite unrealistic to proceed in such a direction.

In addition to aforementioned work, MIT has contributed to, or led, other experimental investigations integral to FSC objectives. In the area of fuel assembly, for example, MIT has measured or will measure ρR and ρR asymmetries of the assembled mass in high-ρR experiments, such as those of Betti and Zhou and Stoeckl that are planned for early 2006. MIT has already done similar ρR and ρR asymmetry measurements in support of the "cone-capsule" fuel assembly experiments of Stephens et al, and of Stoeckl et al. In addition, MIT has recently developed a unique diagnostic that images the fusion burn, and has applied this technique to shimmed targets. Given the innate asymmetry in cone-in-shell implosions, shimmed targets that partially compensate for the drive asymmetry, might, for example, find useful application. Furthermore, as discussed herein, fusion burn images are the "Admiral's test" of the combined processes of drive, mix, fuel assembly, and burn.

Another area of investigation concerns the generation of magnetic and electric fields by the interaction of laser beams with matter, an example of HED Physics and Extreme states of matter, which too is one of the premier goals of the FSC. To sensitively probe these fields, MIT has developed a novel monoenergetic proton source, a result of imploding a capsule with D^3He fuel with a small number of laser beams at OMEGA; fusion products include 14.7-MeV D^3He protons and 3.0-MeV DD protons, both of which are then used to simultaneously probe time-dependent B and E fields resulting from laser-matter interactions. Such monoenergetic sources have distinct advantages over broad-band proton sources associated with intense-laser-beam experiments. To explore these field generation processes, MIT has full days of OMEGA shots in February and August, 2006. In addition, this type of backlighting with 14.7-MeV protons leads in a natural way to the radiographing of implosions, the aim of which would be to fully characterize the assembled mass and its ρR distribution. MIT and colleagues are contemplating such experiments at the OMEGA facility, where, with 60 beams, both backlighting and implosions can occur simultaneously.

Education and training of students and young researchers comprises an important goal of the FSC. To that end, MIT, along with all other FSC members, helped in the organization and implementation of the very successful summer school in high-energy density physics. MIT sent 4 PHD students to this summer school and two of them, Mr. Cliff Chen and Mr. Daniel Casey, have been actively involved in the research leading to this report.

Finally, in Section 6 a detailed work plan for the next three years is presented.

TABLE OF CONTENTS

LIST OF FIGURES

LIST OF TABLES

1. ELECTRON TRANSPORT AS IT RELATES TO FI AND PREHEAT

A. Description of the model

A basic problem in plasma physics, with applications to Fast Ignition [1] and to fuel preheat [2] , is the energy deposition of energetic charged particles into a dense plasma. A fundamental difference exists, however, between energetic electron and ion stopping, in that the profound effects of electron scattering [3], which manifest themselves in pronounced straggling and blooming, needs to be treated in the energy deposition. This scattering, present for both plasma and cold matter, but, until recently, only treated analytically in the latter case [4], is illustrated in Fig. 1.

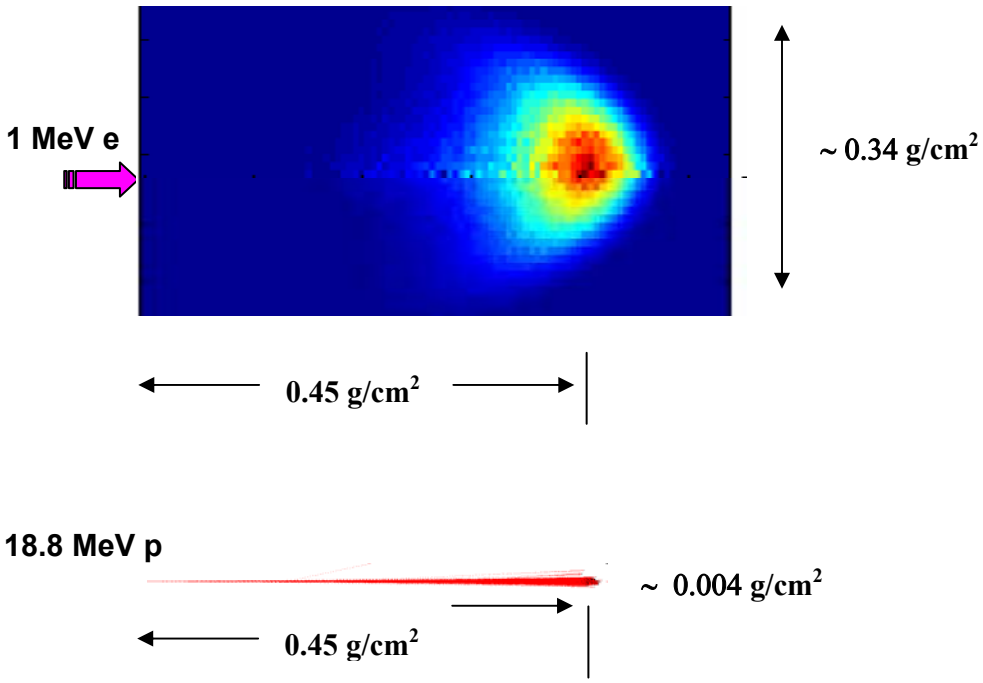

FIG. 1. Illustrated here is the pronounced difference in blooming and straggling, a consequence of scattering effects, for equally penetrating electrons and protons (mean penetration of 0.45 g/cm^2) into DT ice of 0.25 g/cc. Both cold matter and CELSA model calculations, though differing in specific details, display this same general behavior, i.e. both find the electron blooming (or straggling) is ~ 100 times that of the protons.

As noted in Fig. 1, straggling and and blooming for equally penetrating electrons and protons, is ~ 100 times larger for electrons. And for the case of 1-MeV and lower energy electrons, blooming and straggling are always a significant fraction of the penetration (ρX), with, in fact, the ratio of blooming (or straggling) to penetration (ρX) significantly increasing as the energy decreases.

With these issues in mind, C. K. Li and coworkers recently developed a model of energetic electron stopping which couples together both scattering and energy loss as the electrons slow in the background plasma [5-7]. (Details of the calculations, referred to henceforth as Coupled Energy Loss and Scattering Analysis, or CELSA, are contained in those

references.) In brief, whenever $\lambda_D < r_g$, $L_{||} >> \lambda$, and $L_\perp >> \sqrt{\lambda r_g}$, with λ_D the Debye length, r_g the gryo radius (due to, e.g. current flows), λ the mean free path, and $L_{||}$ and $L_\perp$ the longitudinal and lateral plasma scale lengths [8], the interaction of the energetic electrons are dominated by classical coulomb collisions, thus collisional transport processes prevail. For the case of fast ignition, Fig. 2 illustrates the regimes in the interior of the compressed capsule ($n_e \geq 10^{24}$/cc) where collisional transport dominates and, in contradistinction, near the surface of the capsule where Weibel-like instabilities and large self-magnetic field effects dominate electron transport. For the case of preheat, which affects the fuel assembly through the adiabat, collisional transport of the CELSA model is solely important.

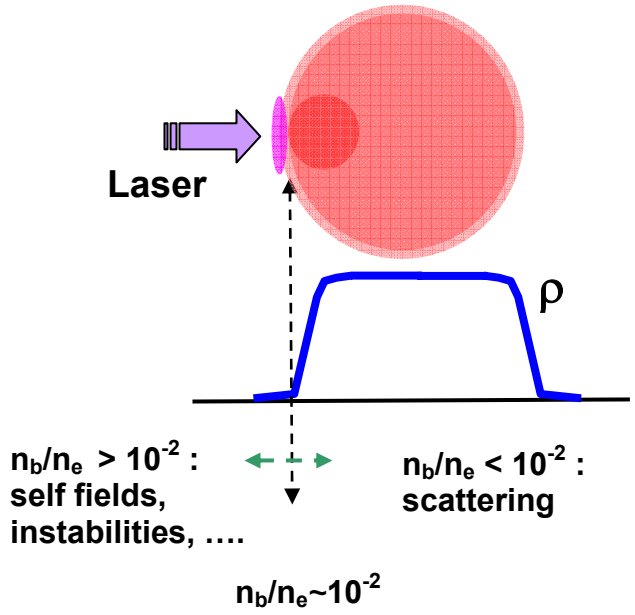

FIG. 2. Schematic illustration of MeV electron transport and energy deposition in a pre-compressed target. Two distinct regions for electron transport are illustrated: First, when $n_b/n_e > 10^{-2}$, electron transport is highly filamented due to Weibel-like instabilities which dominate energy loss and beam blooming; however, for $n_b/n_e < 10^{-2}$, for which λ_D is clearly smaller than the energetic electron gyro radius associated with the beam current, Weibel-like instabilities are stabilized and the electrons are then subject to the scattering, straggling, and blooming processes described by the CELSA model.

B. Predictions of the model

With the previous considerations in mind, results are illustrated by applying the CELSA model to FI and preheat scenarios. Figure 3 illustrates the stopping power for 1 MeV electrons slowing in a 300 g/cc DT plasma. The non-scattering or "uniform" energy deposition model used, for example, by Atzeni [9] lacks the enhanced region of energy deposition, a result of straggling and blooming; furthermore, the mean penetration of the non-scattering model is about 30% farther, a natural consequence that the (non-physical) straight-line approximation for the electron path suffers no deflections while slowing.

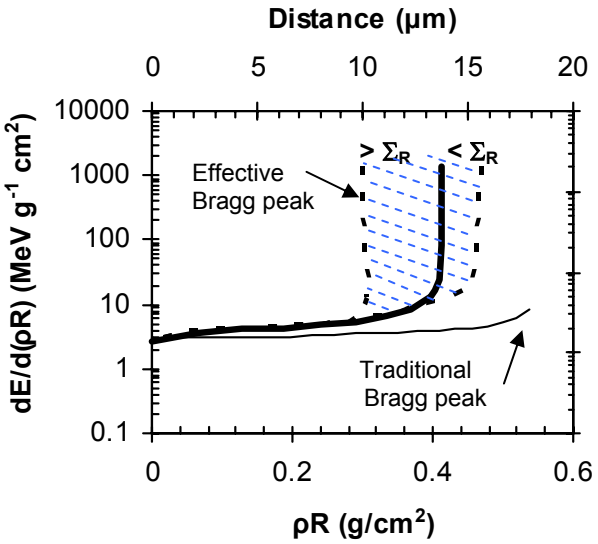

FIG. 3. The stopping power plotted as a function of the electron penetration for 1-MeV electrons in a DT plasma (ρ=300g/cm^3 and T_e=5 keV). The heavy solid line represents the mean energy loss, while the two dashed lines schematically indicate the straggling range over which energy is effectively spread. The thin line illustrates the continuous slowing-down approximation, or non-scattering model, of energy desposition.

In order to more fully explore the consequences of the CELSA model for 1-MeV electrons, Fig. 4 plots, utilizing the results of Fig. 3, the energy deposition into a uniform 300g/cc DT plasma for electron beam footprints with radii from 1 to 20 μm.

Also plotted are the results of the non-scattering model similar to that used by Atzeni [9]. In each case, the model deposition profiles are usually quite different, the consequence of which would be to modify, in a fashion yet to be determined (Section 6), the ignition conditions discussed by Atzeni [9].

These considerations, especially the mean penetration (ρX), are also potentially important for the electron preheat problem [2] which, if excessive, could raise the fuel adiabat and preclude proper fuel assembly. Table I tabulates the results of the CELSA model for conditions applicable to preheat, ie. densities near or a few times above solid DT, plasma temperatures of ~ 10 eV, and electrons with energies from ~ 10 to ~100 keV. The materials listed in Table 1 (CH, Be, or DT) are either being used at OMEGA in current experiments, will be used in the near future at OMEGA, or will be used for the NIF ignition experiments. Figure 5 shows the mean penetration ($\rho\langle x\rangle$) of the CELSA model as function of the electron energy, where the DT ice thickness for the direct drive capsule, as noted, is approximately 350 μm or ~ 9 mg/cm^2. While 100 keV electrons are seen to penetrate ~ 8 mg/cm^2, electrons of substantially smaller energy will, of course, wreak significant damage on the fuel adiabat if sufficient in numbers. To this point, work that remains (Section 6) is to convolve conceivable or expected electron distributions with these stopping power calculations, and to calculate the resultant adiabat. The effects on the fuel assembly can then be quantitatively assessed.

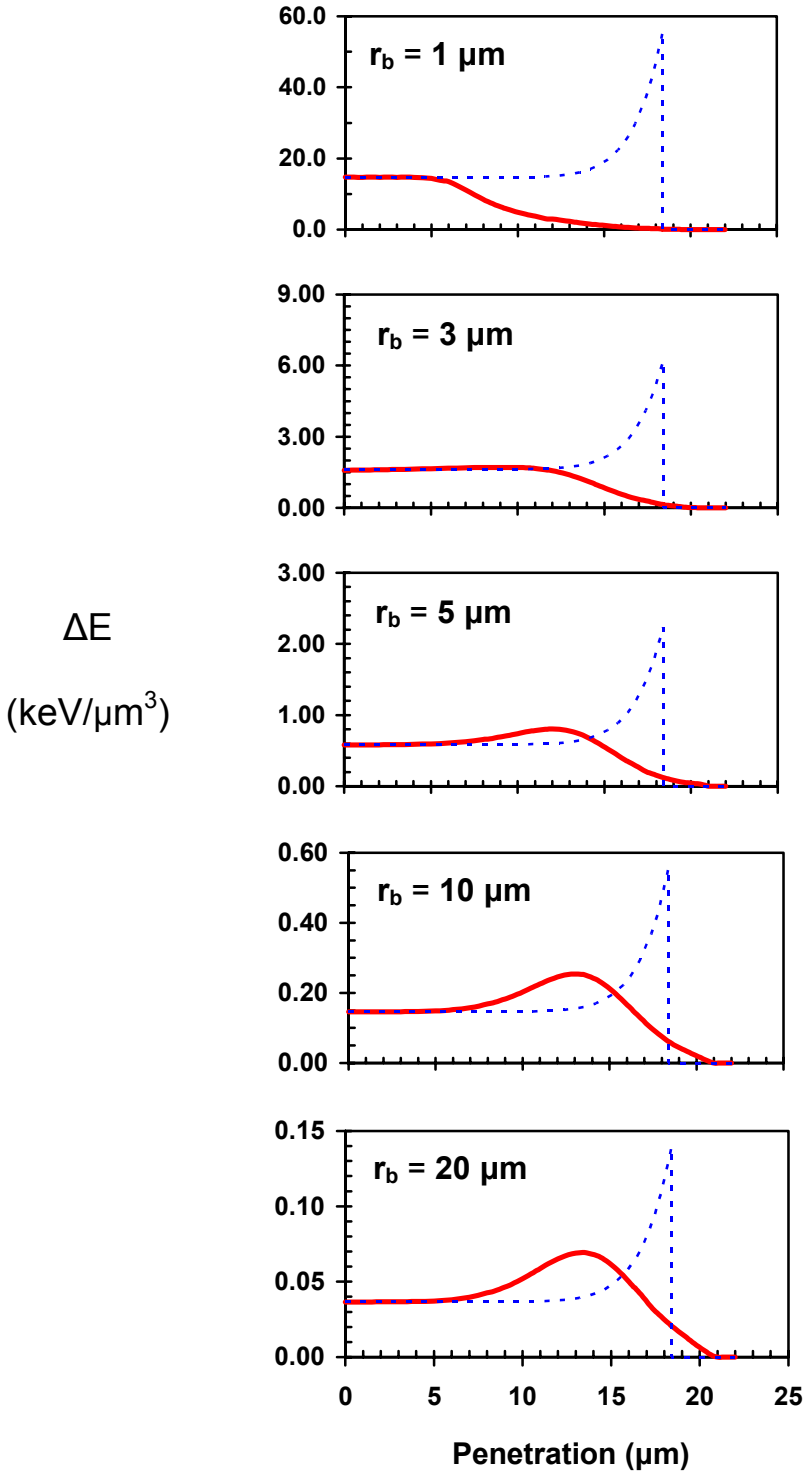

FIG. 4. Energy deposition profiles calculated using the CELSA model (solid line) and a "uniform" energy deposition model, similar to that used by Atzeni [9]. The radii of the beam footprint for the 1 MeV electrons varies from 1 to 20 μm. In nearly every case, significant differences exist between the two model energy deposition profiles, the consequence of which is likely to affect details of the ignition criteria.

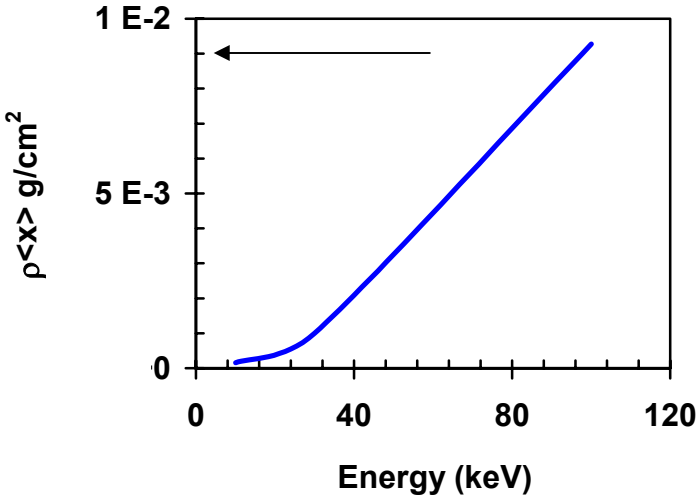

FIG. 5. The penetration of electrons, with energies between 10 and 100 keV, into a DT plasma of 0.25 g/cc and ~ 10 eV. Increasing the plasma density to 1 g/cc, as might occur after passage of a strong shock, has a small effect on these results (Table I). For the NIF direct drive capsule, the DT ice thickness corresponds to an areal density of 9 mg/cm^2, as indicated by the arrow.

TABLE I. Interactions of 10-keV and 100-keV electrons with DT, Be and plastic CH plasmas, common ablator or fuel materials of ICF. The plasma T_e ~10eV. (For CH, the scattering effects are calculated for carbon ions and all plasma electrons). $\rho\langle x\rangle$ or $\langle x\rangle$ is the mean penetration, Σ_R (Σ_B) is the associated straggling (blooming). For fixed energy, $\Sigma_B/\langle x\rangle$ increases with Z.

E_0		ρ	R	$\langle x\rangle$	$\rho\langle x\rangle$	Σ_R	Σ_B	$\frac{\Sigma_R}{\langle x\rangle}$	$\frac{\Sigma_B}{\langle x\rangle}$
(keV)		(g/cm^3)	(μm)	(μm)	(g/cm^2)	(μm)	(μm)		
10	DT	0.25	6.0	4.72	1.2×10^{-4}	1.09	1.60	0.23	0.33
		1.0	1.67	1.35	1.4×10^{-4}	0.31	0.44	0.23	0.32
	Be	1.85	0.84	0.57	1.1×10^{-4}	0.18	0.24	0.31	0.42
		7.4	0.23	0.16	1.2×10^{-4}	0.05	0.067	0.31	0.42
	CH	1.0	1.16	0.72	7.2×10^{-5}	0.26	0.35	0.36	0.48
		4.0	0.32	0.21	8.4×10^{-5}	0.076	0.10	0.36	0.48
100	DT	0.25	330	283	7.1×10^{-3}	42.8	75.4	0.15	0.27
		1.0	86.0	75.0	7.5×10^{-3}	11.1	19.1	0.15	0.26
	Be	1.85	43.0	31.0	5.7×10^{-3}	8.17	12.1	0.26	0.39
		7.4	11.3	8.5	6.2×10^{-3}	2.20	3.27	0.26	0.38
	CH	1.0	59.7	42.4	4.2×10^{-3}	13.6	17.2	0.32	0.41
		4.0	15.6	11.0	4.4×10^{-3}	3.57	4.49	0.32	0.41

2. COMPARISON OF CELSA TO COLD MATTER CALCULATIONS

The CELSA plasma model has been compared to Monte Carlo simulations of electron transport in cold matter in order to better understand the differences and similarities between the two. Monte Carlo simulations were performed using the Integrated Tiger Series version 3.0 (ITS 3.0) developed at Sandia National Laboratories. The ITS electron-photon transport packages has been well validated.

ITS simulations have been run to compare, in particular, the results of cold matter penetration, straggling, and blooming to the corresponding predictions of the CELSA model. Figure 6 pictorially depicts the transport endpoints of a 100 keV electron beam in plasmas and in cold matter. We see that the electron range in solids is about 50% larger than that in plasmas. Blooming and straggling are also scaled accordingly.

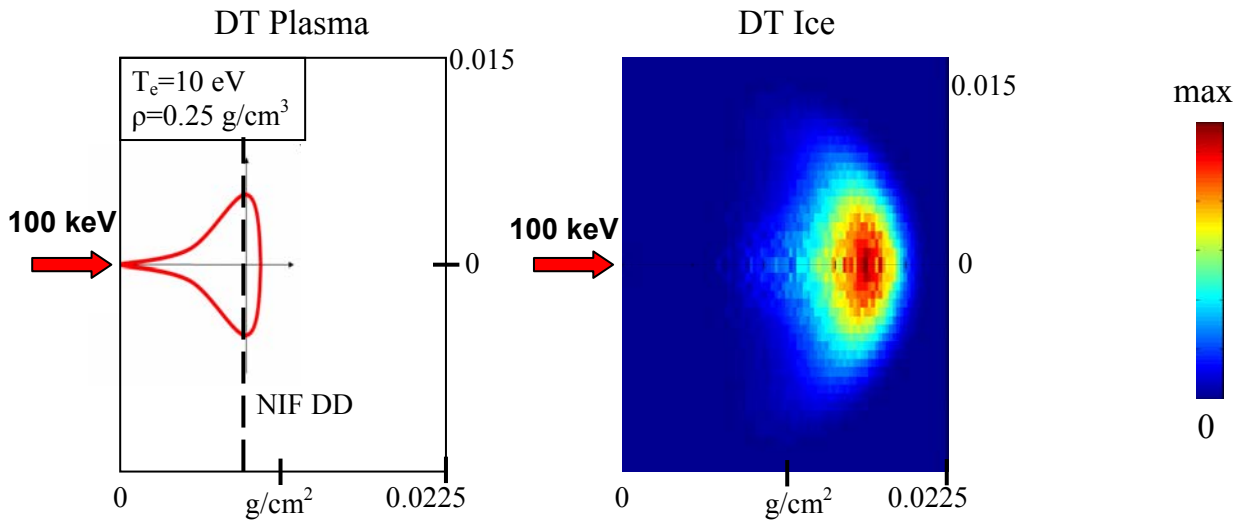

FIG. 6. A near apples-to-apples comparison between CELSA and cold matter stopping for 100 keV electrons. The cold matter is DT ice at 0.25 g/cc. The DT plasma also has density of 0.25 g/cc, but a temperature of ~ 10 eV. For the plasma, the electron penetration is about 50% smaller. The dashed vertical line (left figure) corresponds to the areal density of the NIF direct drive DT ice.

The two primary differences between plasma and cold matter transport lie in the stopping powers and in the collisional scattering. For the stopping power, the energy loss in solids is primarily due to inelastic collisions with atomic electrons (and bremsstrahlung for higher energy electrons), whereas for plasmas energy loss is due to binary collisions with electrons and plasma oscillations (which contribute about 15%). The stopping power is shown in Fig. 7. The plasma stopping power for DT is higher than the corresponding Berger-Seltzer stopping power in cold matter by about 30%. In a near apples-to-apples comparison between DT plasmas and DT ice, Fig. 8 shows that the penetration in solids is about 50% higher in solids than in plasmas from about 10 keV up to a few MeV (narrowing beyond that). This difference can be attributed to the higher stopping power of plasmas and to differences in the effects of scattering in the two mediums.

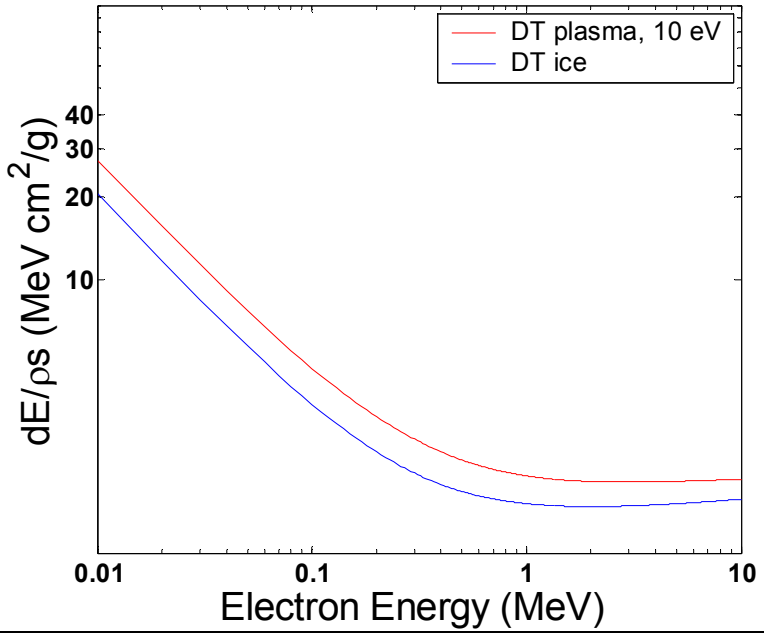

FIG. 7. A comparison of the plasma stopping power for 10 eV, DT plasma and that of DT ice; both materials have a density of 0.25 g/cc. The plasma stopping power [5] is about 30% larger than that of the ice [10]. Plasma oscillations can only account for about half of this difference.

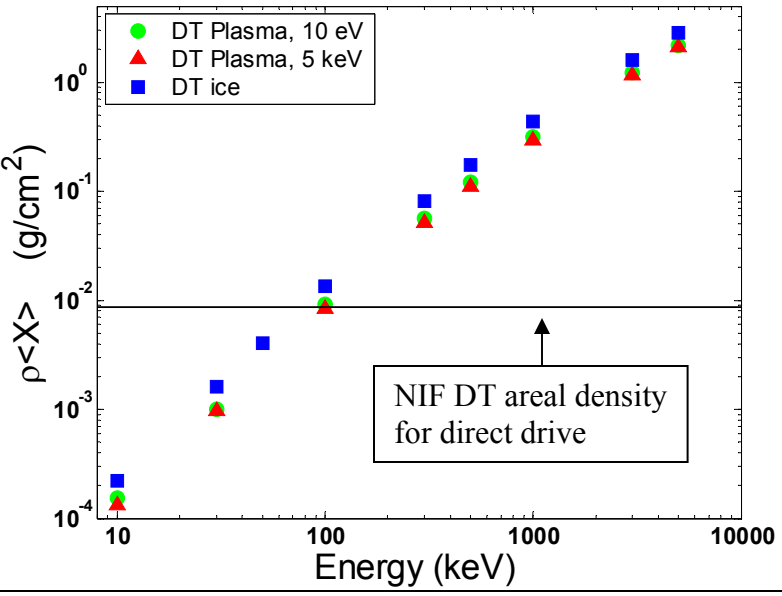

FIG. 8. A near apples-to-apples comparison between CELSA and cold matter stopping for 10 keV to 10 MeV electrons. The cold matter is DT ice at 0.25 g/cc. The DT plasma also has density of 0.25 g/cc, but a temperature of either ~ 10 eV or 5 keV. Up to about 1 MeV, the plasma penetration for the fast electrons is about 50% smaller.

Figure 9 depicts the strong Z dependence of electron transport in cold matter for DT ice, Be, and Cu. Not surprisingly, the larger the Z, the smaller the penetration, and the larger the ratio of blooming (or straggling) to penetration. Although details differed for the plasma calculations, the same qualitative trends were also observed (Table II).

As gold cones are contemplated for use in fast ignitor experiments, Fig. 10 compares the electron transport in DT and in gold. The scattering effects for Au are quite pronounced. Thus even small quantities of Au inadvertently injected into the compressed capsule during fuel assembly could have serious consequences for the transport of the FI electron beam.

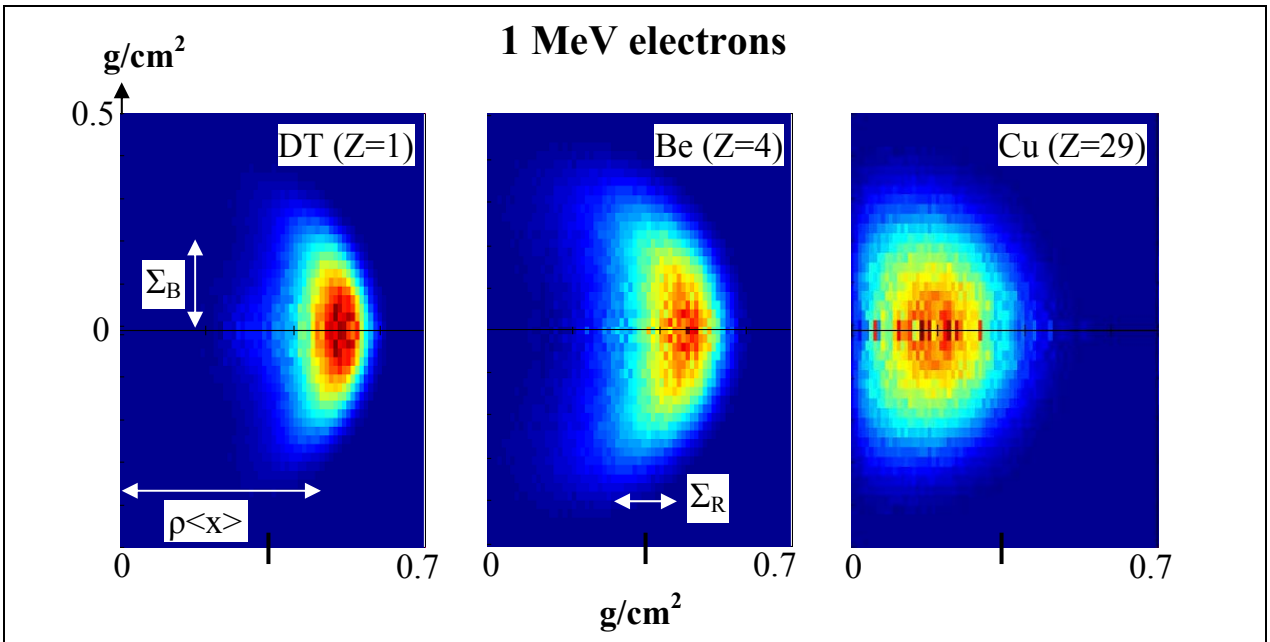

FIG. 9. Electron transport and scattering effects in cold material are a strong function of the atomic number, as illustrated here for DT ice, for Be, and for Cu. As illustrated, the ratio of blooming to penetration increases strongly as the Z increases. This property was also found for the plasma calculations, as illustrated in Table II for the same materials. Differences exist, however, in the details of the two sets of calculations.

TABLE II. Interactions of 1 MeV electrons with DT, beryllium, aluminum and copper plasmas, assuming plasma T_e= 5 keV and n_e=7.2×10^{25} in every cases. For Cu plasma, bremsstrahlung loses are about 5%, and are ignored. As in cold matter, $\Sigma_B/\langle x\rangle$ increases significantly with Z.

Z	ρ (g/cm^3)	R (μm)	$\langle x\rangle$ (μm)	ρ$\langle x\rangle$ (g/cm^2)	Σ_R (μm)	Σ_B (μm)	$\frac{\Sigma_R}{\langle x\rangle}$	$\frac{\Sigma_B}{\langle x\rangle}$
1	300	17.9	13.9	0.42	2.7	4.7	0.19	0.33
4	271	17.9	10.6	0.29	3.8	5.4	0.36	0.51
13	249	17.9	6.3	0.16	4.2	5.1	0.67	0.81
29	265	17.9	3.7	0.10	3.7	4.2	1.0	1.14

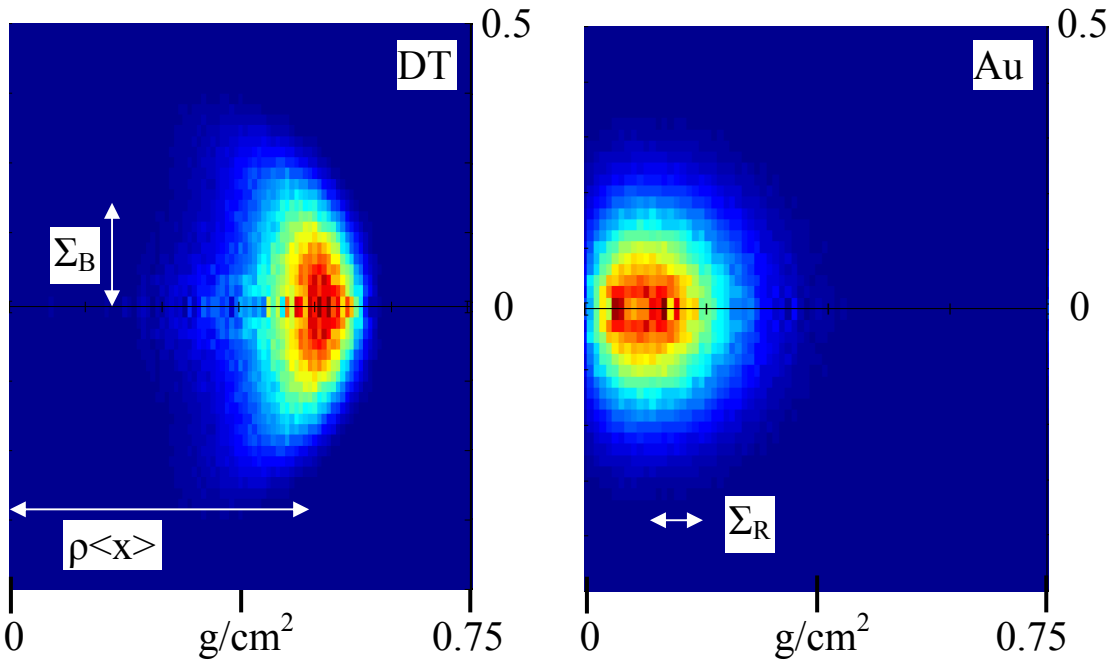

FIG. 10. Comparison of electron transport in DT ice and in Au. The blooming (or straggling) to penetration ratio is dramatically larger for Au. As gold cones are used in FI cone-in-shell fuel assembly experiments [11,12], it is important that small amounts of Au are not inadvertently injected into the fuel during compression, not only because of excessive radiation loss, but because of enhanced scattering that could adversely affect the deposition profile of the ensuing FI electron beam.

3. CONSIDERATION OF A COLD MATTER STOPPING EXPERIMENT FOR TESTING THE CELSA MODEL

Both preheat and FI ignition scenarios involve important issues regarding energy deposition of energetic electrons in a plasma, either near solid densities, in the case of preheat, or at ~ 300g/cc, for the case of FI. A serious question which MIT addressed, with the assistance of the Electron Transport Task Force (ETTF), is whether a definitive experiment could be done to test the CELSA model of energy deposition in plasmas. First, fundamental plasma stopping experiments are notoriously difficult to do, and that is even the case for ion stopping, which, because of small scattering effects (see Fig. 1), is orders of magnitude easier to accomplish than any experiment that contemplates the study of electron stopping. Given this situation, MIT considered whether any realistic electron stopping experiment could be done in cold matter that would shed light or insight on the veracity of the CELSA model. In this consideration, two issues arose: First, would we be able to convincingly demonstrate that a proof of cold-matter stopping, beyond that which already exists in the literature, would unambiguously prove the veracity of the CELSA model? Despite the fact that there are many common elements of the two approaches, such as each includes the crucial effects of scattering, there remain fundamental differences, such as plasma screening effects. Our conclusion was that any such inferences would, at best, be on inconclusive grounds.

A second important issue was that given that the literature and work on electron stopping in cold matter is so extensive and exhaustive [4, 13], is there any experiment that MIT could do, or lead for the ETTF or the FSC , that would extend our understanding, in a fundamental way, of straggling and blooming processes in cold matter? To this second question, we remain skeptical that, without a vast expenditure of resources, far beyond what is reasonably available within the FSC budget, that such is doable. We came to this conclusion reluctantly, and after considerable work and research into this topic.

4. EXPERIMENTS ON FUEL ASSEMBLY: ρR AND ρR ASYMMETRIES AND FUSION BURN IMAGING

A. Experiment on ρR asymmetries of mass assembly in cone-in-shell implosions

The reentrant cone-in-shell concept [14-16] is a novel approach to fast ignition (FI) [1], separating fuel-assembly from fuel heating by combining a driver that compresses the fuel to high density with an ultra-fast laser for heating. Charged-particle diagnostics are playing a unique role in assessing the mass assembly by measuring ρR and ρR asymmetries, as demonstrated by recent experiments at OMEGA [11]. Figure 11 shows, at time of peak proton production, an image of an imploded 10-atm D^3He-filled cone target made with a 6.7-keV x-ray backlighter. The measured energy loss of 14.7-MeV D^3He protons was used to infer the ρR of the compressed capsule [24] in different directions. The narrow peak seen at the high-energy end of the spectra is attributed to the shock phase of the implosions, at which time the assembled ρR is low. At lower energies, there is a second broad peak attributed to the compression phase of the implosion. Of the five views of this implosion, TIM3 shows the largest compression downshift (~2 MeV), corresponding to ρR = 60±10 mg/cm^2. These measurements quantitatively demonstrate the anisotropy in the mass assembly. We intend to collaborate on the GA- and LLE-led experiments by measuring anisotropies in ρR to address several important issues. These include the effects of changing the cone angle; the effects of mix between the gold cone and the fuel/shell material; the effects of gas pressure; and the effects of cone erosion (due to pressure from the core plasma).

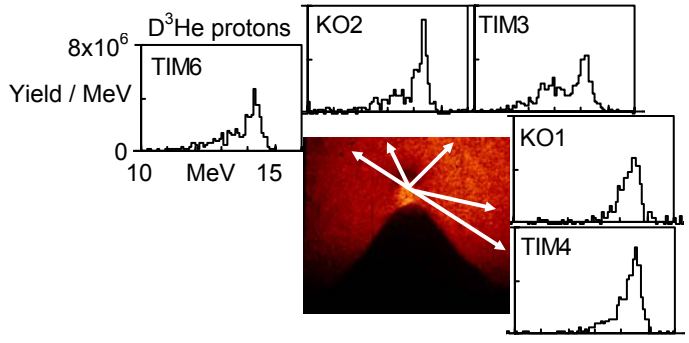

FIG. 11. D^3He proton spectra obtained along 5 different lines of sight for a 10-atm D^3He-filled cone-in-shell implosion indicate ρR asymmetries, with the largest compression ρR in the direction of TIM3 (60±10 mg/cm^2). The x-ray image is a result of a 6.7-keV x-ray backlighter and plasma self emission.

B. Proposed radiography of FI implosions for measuring ρR and radial structure

14.7 MeV D-^{3}He protons generated within implosions have been used extensively to study ρR and its angular variations [17-35], because a spectral measurement at each angle implies a radially-integrated ρR. Such measurements provide no information about radial variations in ρ, but radial information could be obtained by *radiographing* an imploded (H-filled) capsule with protons emitted from a "backlighter" source. Unlike x-rays, energetic protons are largely insensitive to plasma temperature but are sensitive to areal density variations [36] and to electric/magnetic fields [37,38]; proton radiography would therefore be a unique diagnostic for probing both mass distributions in imploded capsules and (with less energetic probe particles) fields outside capsules.

We envision three possible types of backlighter. The first is a capsule implosion, driven with a small number of OMEGA beams (say 20), with remaining beams driving the diagnosed

target implosion; this would produce a nearly monoenergetic source of 14.7-MeV protons that would pass through the compressed target, allowing measurement of $\int \rho\, d\ell$ along different paths and filling in the radial information that has so far been missing. The second is a foil illuminated by a few of the OMEGA beams; this would produce lower-energy "ablator" ions (energies ≤ 1.5 MeV) [18], which would be useful for probing fields outside the imploded capsule. The third is a foil illuminated by a short (1-100 ps), high-intensity ($<10^{20}$ W/cm^2) OMEGA EP pulse, which would produce protons with energies up to ~50 MeV for radiographing capsule structure and density perturbations as well as electric/magnetic fields (around a capsule or inside a hohlraum). The relative timing of the primary implosion and the backlighter implosion can be adjusted; similar experiments with different timing would then give time-evolution information.

We recently conducted the first experiments to demonstrate radiography on OMEGA, using 14.7-MeV protons from capsule implosions to probe E and B fields due to laser-plasma interactions, as described in the next section. Figure 12 illustrates the principle of using higher energy protons from interactions of the OMEGA EP laser with a foil. Such protons might be used to radiograph implosions in FI experiments at OMEGA using, for example, the target design shown in Fig. 13.

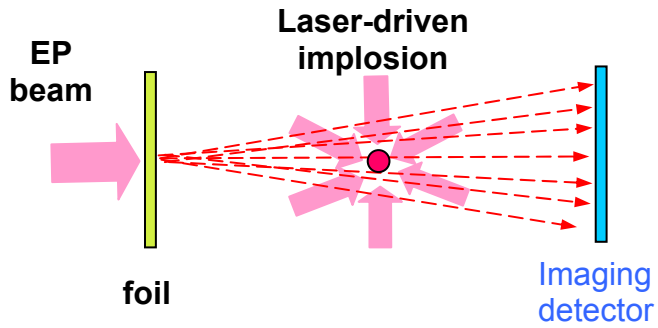

FIG. 12. Schematic diagram of an experiment for imaging the mass distribution in an imploding capsule using high energy protons generated by the interaction of an OMEGA EP laser beam (1 to 100 ps duration, ~10-μm spot size) and a foil.

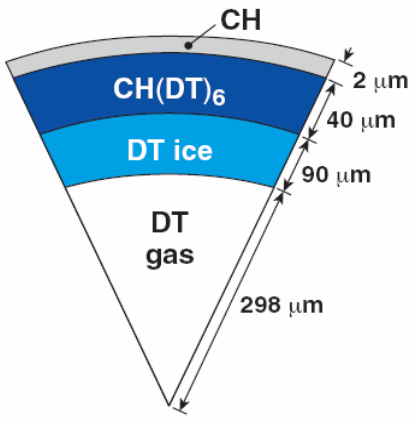

FIG. 13. Capsule structure proposed for FI experiments at OMEGA [39].

C. Proton emission imaging of core asymmetry resulting from drive asymmetry

Measured burn images and burn profiles provide compelling insight into implosion dynamics, including the combined effects of mix, hydro efficiency, and electron and radiation transport. To that end, we developed the multi-camera Proton Core Imaging System (PCIS) [40,41] on OMEGA (Fig. 14) for quantitative, 3-D spatial measurements of the fusion burn region in direct-drive implosions of D^3He-filled capsules. Images from three orthogonal penumbral imaging cameras are processed with special algorithms [40] to produce either the surface brightness of the burn region with arbitrary asymmetric structure [40,42,43] or the radial profile of D^3He reactions per unit volume when burn is spherically symmetric [40,44]. Figure 14 shows an example of how (intentionally) asymmetric laser drive results in an asymmetric burn region. Similar results for different types and amplitudes of drive asymmetry show clear correlations between drive conditions, the shimming of targets, and burn asymmetries.

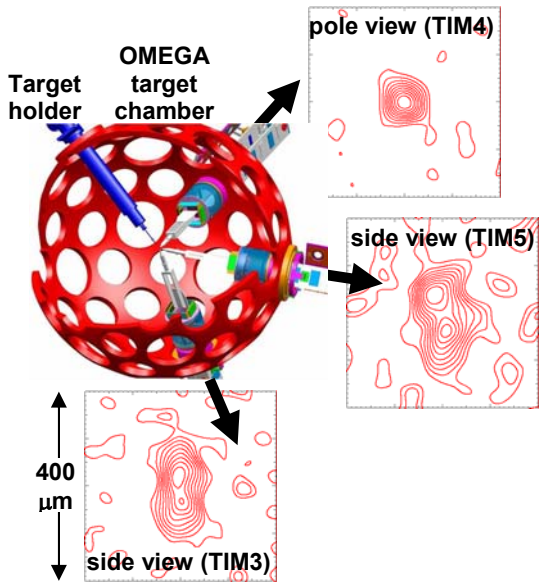

FIG. 14. 3-D imaging of D^3He burn in an asymmetric OMEGA implosion (Shot 31752) shows the effects of drive asymmetry. The contour plots show surface brightness of the burn region as seen simultaneously from three orthogonal directions by separate proton emission cameras [40,41]. Prolate burn asymmetry resulted from (intentional) laser drive asymmetry with lower than average illumination in two opposing directions. The pole view is along the axis of symmetry, both side views are orthogonal to it. These kinds of burn images constitute the "Admiral's Test" in that they are exacting tests of 2- and 3-D integrated simulations of the entire implosion process, including drive, mix, fuel assembly, and burn.

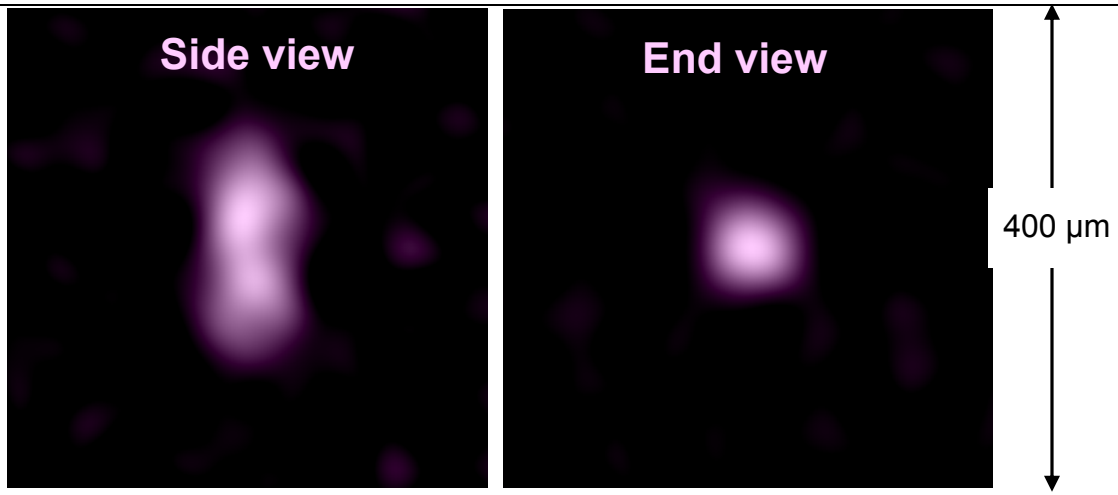

FIG. 15. The "side"(TIM3) and "end" view images of Fig. 14 shown as grey-scale images.

5. EXPERIMENTS ON E- AND B-FIELD GENERATION BY LASER-PLASMA INTERACTIONS

As part of the NLUF program at OMEGA, MIT took the first preliminary data in an ongoing series of experiments using proton radiography to study Transient E and B fields generated by the interaction of OMEGA laser beams with plastic foils. In each experiment a plastic foil was illuminated by a single OMEGA laser beam, and projection radiographs were made of the foil using a backlighter providing monoenergetic 14.7-MeV protons and 3-MeV DD protons; the image recorder was a CR-39 area detector. The protons passed through a wire mesh before impinging on the foil, and the distortion in the mesh pattern at the detector shows how the proton trajectories were deflected through interaction with the fields generated by laser-plasma interaction at the foil. Figures 16 and 17 show the experimental setup. The backlighter was formed by imploding a D^3He-filled, glass-shell capsule with 20 OMEGA laser beams in a 10-kJ, 1-ns pulse. The capsule diameter used was unusually small, at about 440 µm, in order to provide a smaller-than-usual burn radius for optimal spatial resolution in the radiograph; the FWHM of the proton source was measured with proton emission imaging to be about 50 µm. The mesh was mounted on the foil assembly about 1 cm away, and the center-to-center spacing of the mesh wires was either 150 µm or 200 µm. The diameter of the laser beam incident on the foil was 800 µm, and the laser intensity was about 10^{14} W/cm^2, and the pulse length was 1 ns. The CR-39 detector was about 36 cm away. Since the burn duration of the D^3He implosion was short (~ 150 ps) relative to the duration of the foil illumination, and since the relative timing of the implosion and the foil illumination was adjustable, it was possible to record images at different times relative to the foil illumination.

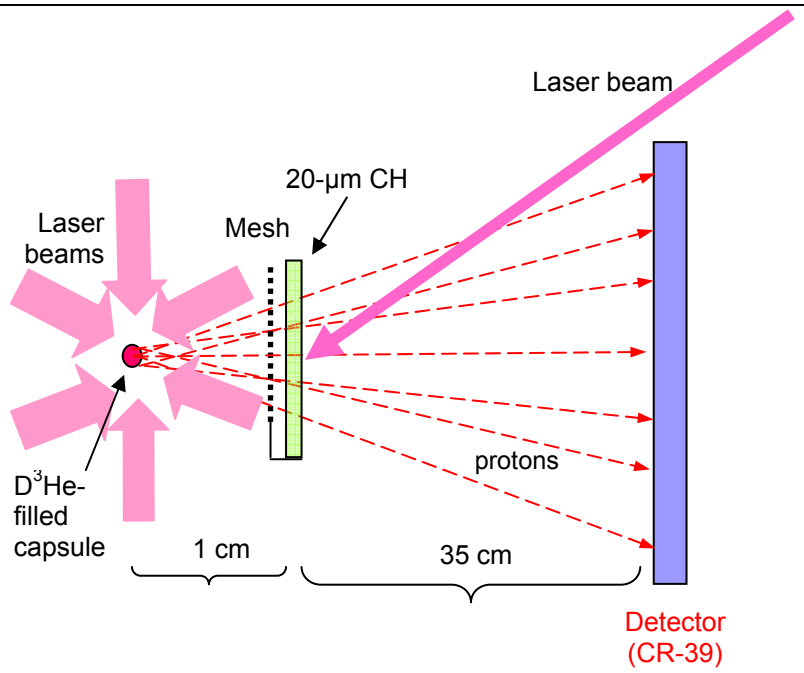

FIG. 16. Physical arrangement of the proton backlighter (imploded D^3He-filled capsule), mesh, CH foil, CR-39 imaging detector, and OMEGA laser beams, as used for radiography.

FIG. 17. Photograph taken before an actual experiment, showing the backlighter capsule (left), the CH foil (right), and the wire mesh (just to the left of the foil).

Sample images recorded at different times are shown in Fig. 18. These images are currently being analyzed in collaboration with LLE and LLNL coworkers in order to provide information about the time evolution of the field-induced distortion. Preliminary results are shown in Fig.19. Qualitatively, at least, they agree with LASNEX simulations that indicate formation of a plasma "bubble" with B field of ~ 0.5 MG at t = 0.5 ns [45]. MIT plans to extend these measurements.

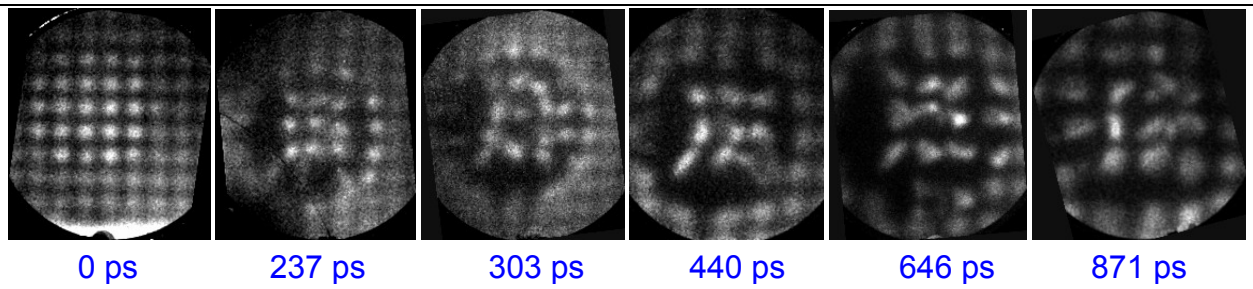

FIG.18. Images recorded on the CR-39 detectors during different OMEGA shots. Each image is labeled by the difference between the time at which the protons passed the foil and the time when the foil was struck by a laser beam. The first three images were made using a mesh with 150-μm (center-to-center) spacing, while the last three were made with a 200-μm mesh.

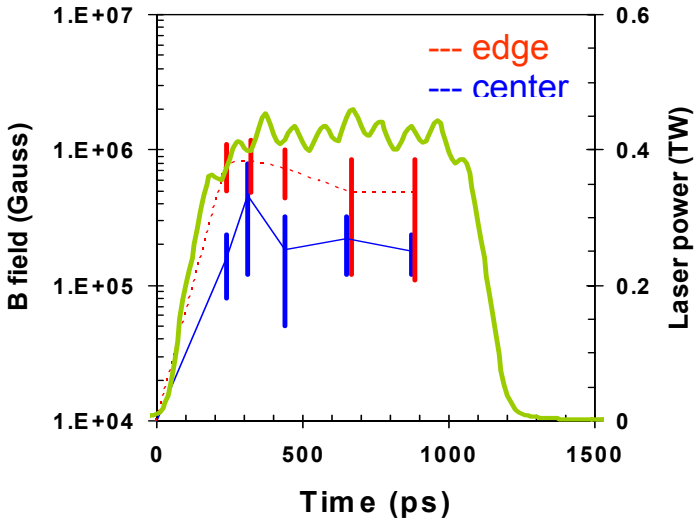

FIG. 19. Preliminary time evolution of B-field strength near the center and near the edge of the footprint of the laser beam on the CH foil, deduced from distortions in the proton-beam images shown in Fig. 18.

6. WORK PLAN FOR 2006, 2007, AND 2008

A. Extend theoretical and numerical efforts

- Complete calculations of energy deposition of MeV electron for fast ignition isochoric experiments (assuming uniform density and temperature profiles). Determine ignition criteria.
- Calculate energy deposition of MeV electron for fast ignition experiments on OMEGA/OMEGA EP (using simulated density and temperature profiles from J. Delettrez and R. Betti). Determine ignition criteria.
- Calculate energy deposition of MeV electron for fast ignition experiments on the NIF (using simulated density and temperature profiles from R. Betti and others). Determine ignition criteria.
- Using different energetic electron distributions for the FI electron beam, determine the energy deposition profiles for the above cases. Establish the sensitivity of ignition criteria on the electron distribution.
- For preheat, convolve conceivable or expected electron distributions with stopping power calculations; calculate resultant adiabat. Assess effects on fuel assembly.
- Submit papers on these efforts, report results at conferences

B. Experiments in fuel assembly: ρR and ρR asymmetries and fusion burn images

- Using charged-particle spectrometers, measure ρR and ρR asymmetries of the assembled mass for high-ρR experiments of Betti and Zhou and Stoeckl of LLE, and for cone-in-shell experiments.
- Explore the use of proton radiography, utilizing implosions from D^3He capsules that generate 14.7 MeV protons, for assessing fuel assembly, ρR, and ρR asymmetries.
- Extend fusion burn imaging to assess fuel assembly and burn. Especially explore the utilization of shimmed targets that might compensate for cone-in-shell asymmetries.

C. Experiments in E and B fields generation relevant to HEDP

- Develop and improve proton radiography technique for sensitive E and B fields measurements
- Explore and continue our experiments on OMEGA to measure E and B fields generated by laser-plasma interactions (flat CH foils).
  Two full-day experiments have been planned (Feb. and Aug. 2006)
  (Close collaboration with R. Town, A. MacKinnon, O. Landen of LLNL, and C. Sangster of LLE)
- Extend this technique to E and B field measurements on OMEGA EP.
- Explore proton radiography to study electron transport on OMEGA EP.
- Submit scientific papers and report on these efforts

REFERENCES

1. M. Tabak *et al.,* *Phys. Plasmas* **1**, 1626 (1994).
2. M. D. Rosen, R. H. Price, E. M. Campbell *et al*., *Phys. Rev.* A **36**, 247 (1987).
3. G. Molière, *Z. Naturforsch*, **3a**, 78 (1948).
4. H. A. Bethe, *Phys. Rev*. **89** 1256 (1953).
5. C.K. Li and R.D. Petrasso, "Stopping of Directed Energetic Electrons in High-Temperature Hydrogenic Plasmas" *Phys. Rev*. E, **70**, 067401 (2006).
6. C.K. Li and R.D. Petrasso, "Stopping, Straggling, and Blooming of Directed Energetic Electrons in Hydrogenic and Arbitrary-Z Plasmas", to be published in *Phys. Rev*. E, **73**, January 2006.
7. C.K. Li and R.D. Petrasso, "Energy deposition of MeV electrons in compressed targets of fast-ignition inertial confinement fusion", to be published in *Phys. Plasmas* (2006).
8. B. Trubnikov, *Review of Plasma Physics* 1 (Consultants Bureau, New York, 1965).
9. S. Atzeni, *Phys. Plasmas* **6**, 3316 (1999).
10. M. J. Berger and S. M. Seltzer, National Academy of Science – National Research Council Publication 1133 (1965); L. Pages, E. Bertel, H. Joffre and L. Sklavenitis, Atomic Data **4**, 1-127 (1972), and references therein.
11. C. Stoeckl, T. Boehly, J. Delettrez, S. Hatchett, J. Frenje, V Yu Glebov, C. K. Li, J.E. Miller, R. D. Petrasso, F. H. Séguin, V. Smalymuk, R. Stephens, W. Theorbald, B. Yaakobi, and C. Sangster, *Plasma Phys. Contr. Fusion* **47**, B859 (2005).
12. R. B. Stephens, S. P. Hatchett, R. E. Turner, K. A. Tanaka, and R. Kodama, *Phys. Rev. Lett*. **91**, 185001 (2003)
13. R. D. Evans, *The Atomic Nucleus* (McGraw-Hill, new York, 1955).
14. M. Tabak, LLNL patent, 1997.
15. P. Norreys *et al.*, *Phys. Plasmas* **7**, 3721 (2000).
16. M. H. Key *et al*., *Phys. Plasmas* **5**,1966 (1998).
17. C. K. Li *et al.*, *Phys. Plasmas* **7**, 2578 (2000).
18. D. G. Hicks *et al.*, *Phys. Plasmas* **8**, 606 (2001).
19. R. L. McCrory *et al.*, *Nuclear Fusion* **41**, 1414 (2001).
20. D. D. Meyerhofer *et al.*, *Phys. Plasmas* **8**, 2251 (2001).
21. D. D. Meyerhofer *et al.*, *Plasma Phys. Contr. Fusion* **43**, A277 (2001).
22. F. H. Séguin *et al.*, *Phys. Plasmas* **9**, 2725 (2002).
23. F. H. Séguin *et al.*, *Phys. Plasmas* **9**, 3558 (2002).
24. C. K. Li *et al.*, *Phys. Rev. Lett.* **89**, 165002 (2002).
25. C. Stoeckl *et al.*, *Phys. Plasmas* **9**, 2195 (2002).
26. P. B. Radha *et al.*, *Phys. Plasmas* **9**, 2208 (2002).
27. F. H. Séguin *et al.*, *Rev. Sci. Instrum.* **74**, 975 (2003).
28. T. C. Sangster *et al.*, *Phys. Plasmas* **10**, 1937 (2003).
29. R. D. Petrasso *et al.*, *Phys. Rev. Lett.* **90**, 095002 (2003).
30. V. A. Smalyuk *et al.*, *Phys. Rev. Lett.* **90**, 135002 (2003).
31. C. K. Li *et al.*, *Phys. Plasmas* **10**, 1919 (2003).
32. P. W. McKenty *et al.*, *Phys. Plasmas* **11**, 2790 (2004).
33. C. K. Li *et al*., *Phys. Rev. Lett.* **92**, 205001 (2004).
34. D. C. Wilson *et al.*, *Phys. Plasmas* **11**, 2723 (2004).
35. J. A. Frenje *et al.*, *Phys. Plasmas* **11**, 2798 (2004).
36. C. K. Li *et al.*, *Phys. Rev. Lett.* **70**, 3059 (1993).

37. M. Borghesi *et al.*, *Phys. Rev. Lett.* **92**, 055003 (2004).
38. A. J. Mackinnon *et al.*, *Rev. Sci. Instrum*. **75**, 3531 (2004).
39. R. Betti and C. Zhou, *Bull. Am. Phys. Soc.* **50**, 261 (2005).
40. F. H. Séguin *et al.*, *Rev. Sci. Instrum.* **75**, 3520 (2004).
41. J. D. DeCiantis *et al*., *Rev. Sci. Instrum*., submitted (2005).
42. F. H. Séguin *et al.*, *Bull. Am. Phys. Soc*. **48**, 63 (2004).
43. F. H. Séguin *et al.*, *Phys. Plasmas*, to be submitted.
44. F. H. Séguin *et al*., *Phys. Plasmas*., submitted (2005).
45. R. Town (private communication).

APPENDIX A: PARTICIPANTS IN THE ELECTRON TRANSPORT TASK FORCE

MIT: R.D. Petrasso, C. K. Li, F. H. Seguin, C. Chen, and D. Casey.

LLE: V. Goncharov, O. Gotchev, D. Harding, D. Meyerhofer, J. Myatt, C. Sangster, A. Solodov.

UCSD: F. Beg.

GA: R. Stephens, T. Bernat

OSU: R. Freeman

APPENDIX B: RELATED MIT CONFERENCE PRESENTATIONS

1. C. Chen *et al.,* **"**Comparisons of Electron Transport in Plasmas and in Cold Matter" *47th APS annual meeting***,** Denver, Colorado, *Bull. Am. Phys. Soc.* 50, 293 (2005).

2. R. D. Petrasso *et al*., **"**Penetration, Blooming and Energy Deposition of Energetic Electrons in Preheat Scenarios"**,** *47th APS annual meeting***,** Denver, Colorado, *Bull. Am. Phys. Soc.* 50, 139 (2005).

3. C. K. Li *et al.* "Stopping, Straggling and Blooming of Directed Energetic Electrons in Hydogenic Plasmas"**,** Invited talk, *47th APS annual meeting***,** Denver, Colorado, *Bull. Am. Phys. Soc.* 50, 261 (2005).

4. C. K. Li *et al.,* "Proton radiography of electromagnetic fields generated by laser driven plastic foils ", *47th APS annual meeting*, *Bull. Am. Phys. Soc.* 50, 222 (2005).

5. C. K. Li *et al.,* "Stopping, Straggling and Blooming of Directed Energetic Electrons in Hydogenic Plasmas", *EPS and International Workshop on Fast-ignition*, Torragona, Spain (2005)

6. C. K. Li *et al.,* "Proton radiography of electromagnetic fields generated by laser driven plastic foils--- preliminary analysis", *4th International Conference on Inertial Fusion Science and Application,* Birrertz, France (2005).

7. C. K. Li *et al.,* "Stopping, Straggling and Blooming of Directed Energetic Electrons in Hydogenic Plasmas", *46th APS annual meeting*, *Bull. Am. Phys. Soc.* 49, 103 (2004).

APPENDIX C: RELATED MIT PAPERS

The following papers are attached to this document:

C.K. Li and R.D. Petrasso, "Stopping of Directed Energetic Electrons in High-Temperature Hydrogenic Plasmas" Phys. Rev. E, 70, 067401 (2006).

C.K. Li and R.D. Petrasso, "Stopping, Straggling, and Blooming of Directed Energetic Electrons in Hydrogenic and Arbitrary-Z Plasmas", to be published in Phys. Rev. E, 73, January 2006.

C.K. Li and R.D. Petrasso, "Energy deposition of MeV electrons in compressed targets of fast-ignition inertial confinement fusion", to be published in Physics of Plasmas.

Stopping of directed energetic electrons in high-temperature hydrogenic plasmas

C. K. Li and R. D. Petrasso
Plasma Science and Fusion Center, Massachusetts Institute of Technology, Cambridge, Massachusetts 02139, USA
(Received 26 October 2003; published 10 December 2004)

From fundamental principles, the interaction of directed energetic electrons with a high-temperature hydrogenic plasma is analytically modeled. The randomizing effect of scattering off both plasma ions and electrons is treated from a unified point of view. For electron energies less than 3 MeV, electron scattering is equally important. The net effect of multiple scattering is to reduce the penetration from 0.54 to 0.41 g/cm^2 for 1 MeV electrons in a 300 g/cm^3 plasma at 5 keV. These considerations are relevant to "fast ignition" and to fuel preheat for inertial confinement fusion.

DOI: 10.1103/PhysRevE.70.067401 PACS number(s): 52.40.Mj, 52.25.Tx, 52.50.Gj

A basic problem in plasma physics is the interaction and energy loss of energetic charged particles in plasmas [1–4]. This problem has traditionally focused on ions (i.e., protons, α particles, etc.), either in the context of heating and/or ignition in, for example, inertially confined fusion (ICF) [3–6]; or in the use of these particles for diagnosing implosion dynamics [7]. More recently, prompted in part by the concept of fast ignition for ICF [8], workers have begun considering energy deposition from relativistic fast electrons in deuterium-tritium (DT) plasmas [8–13]. Tabak *et al.* [8] used, for example, the energy deposition of Berger and Seltzer [14] that is based on the continuous slowing down of electrons in cold matter. This treatment, though quite similar to electron slowing in plasmas, does not include the effects of scattering. Deutsch *et al.* [9] addressed this issue by considering the effects of scattering off the background ions [16,17]; they ignored scattering due to background electrons.

In another important context in ICF, workers addressed the issue of fuel preheat due to energetic electrons ($\sim$50–300 keV) [5,18,19], the consequence of which is to elevate the fuel adiabat to levels that would prohibit ignition. Herein we show that scattering effects could be significant for quantitative evaluations of preheat.

The starting point for these calculations is the relativistic elastic differential cross sections for electrons scattering off fully ionized ions of charge Z [20–22], and off the neutralizing bath of electrons [23,21,24], which are approximated as

$$\left(\frac{d\sigma}{d\Omega}\right)^{ei} \approx \frac{Z^2}{4}\left(\frac{r_0}{\gamma\beta^2}\right)^2 \frac{1}{\sin^4(\theta/2)}, \tag{1}$$

$$Z\left(\frac{d\sigma}{d\Omega}\right)^{ee} \approx Z\frac{(\gamma+1)^2}{(2^{\sqrt{(\gamma+1)/2}})^4}\left(\frac{r_0}{\gamma\beta^2}\right)^2 \frac{1}{\sin^4(\theta/2)}, \tag{2}$$

where $\beta=v/c$ and $\gamma=(1-\beta^2)^{-1/2}$; $r_0=e^2/m_0c^2$ is the classical electron radius. The relative importance of electron scattering is implied from the ratio

$$\mathcal{R} = Z\left(\frac{d\sigma}{d\Omega}\right)^{ee} \Bigg/ \left(\frac{d\sigma}{d\Omega}\right)^{ei} \approx \frac{4(\gamma+1)^2}{(2^{\sqrt{(\gamma+1)/2}})^4}\frac{1}{Z}. \tag{3}$$

For a hydrogenic plasma ($Z=1$) and for $\gamma \lesssim 10$, $\mathcal{R}\sim 1$, indicating that the electron component is equally important. As best we can tell, the electron scattering component has been ignored by workers since it was typically assumed, usually justifiably, that ion scattering dominates. However, this will not be the case for problems discussed herein, for relativistic astrophysical jets [25], or for many of the present high-energy laser plasma experiments [26] for which Z is about 1 and for which $\gamma \lesssim 10$.

To calculate the effects of multiple scattering a diffusion equation is used [27],

$$\frac{\partial f}{\partial s} + \mathbf{v}\cdot\boldsymbol{\nabla} f = n_i \int [f(\mathbf{x},\mathbf{v}',s) - f(\mathbf{x},\mathbf{v},s)]\sigma(|\mathbf{v}-\mathbf{v}'|)d\mathbf{v}', \tag{4}$$

where f is the distribution function of the scattered electrons, n_i is the number density of plasma ions of charge Z, $\mathbf{x}$ is the position where scattering occurs, and $\sigma=\sigma_{ei}+Z\sigma_{ee}$ is the total scattering cross section where $\sigma_{ei}=\int(d\sigma/d\Omega)^{ei}d\Omega$ and $\sigma_{ee}=\int(d\sigma/d\Omega)^{ee}d\Omega$. Equation (4) is solved in a cylindrical coordinates with the assumption that the scattering is azimuthally symmetric. The solution that satisfies the boundary conditions is [27,28]

$$f(\theta,s) = \frac{1}{4\pi}\sum_{\ell=0}^{\infty}(2\ell+1)P_\ell(\cos\theta)\exp\left(-\int_0^S \kappa_\ell(s')ds'\right), \tag{5}$$

where $P_\ell(\cos\theta)$ are the Legendre polynomials. Using orthogonality and projecting the $\ell=1$ term,

$$\langle\cos\theta\rangle = \exp\left(-\int_{E_0}^{E}\kappa_1(E)\left(\frac{dE}{ds}\right)^{-1}dE\right), \tag{6}$$

where $\langle\cos\theta\rangle$, a function of the residual electron energy E and the initial energy E_0, is a measure of the mean deflection resulting from multiple scattering [29], and relates dE/ds to dE/dx through

$$\frac{dE}{dx} = \langle\cos\theta\rangle^{-1}\frac{dE}{ds}, \tag{7}$$

where dE/ds is the stopping power along the path while dE/dx is the linear energy stopping power. In the above, $S(E)=\int_0^S ds' = \int_{E_0}^{E}(dE/ds)^{-1}dE$, and

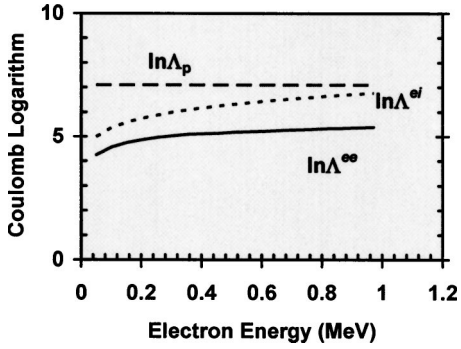

FIG. 1. The Coulomb logarithms for incident 1 MeV electrons interacting with a DT plasma ($\rho=300$ g/cm^3, $T_e=5$ keV). For the background plasma the Coulomb logarithm $\ln \Lambda_p$, which is relevant to plasma transport processes (e.g., electrical and thermal conductivity), is about 7.

$$\kappa_1(E) = 2\pi n_i \int_0^{\pi} \left(\frac{d\sigma}{d\Omega}\right)(1-\cos\theta)\sin\theta\, d\theta, \tag{8}$$

where κ_1 is closely related to the diffusion cross section (or transport cross section) which characterizes the loss of directed electron velocity through scattering [2]. Equations (1) and (2) are substituted into Eq. (8) and, after a standard change of variables, the integrations are taken from $b_{\min}^{ei}$ or $b_{\min}^{ee}$ to λ_D, where λ_D is the Debye length, and $b_{\min}^{ei}$ ($b_{\min}^{ee}$) is the larger of b_q^{ei} (b_q^{ee}) or $b_{\perp}^{ei}$ ($b_{\perp}^{ee}$) [30]. b_q^{ei} and b_q^{ee} are approximately the electron de Broglie wavelength, and $b_{\perp}^{ei} = Zr_0/\gamma\beta^2$ and $b_{\perp}^{ee} \approx 2(\gamma+1)r_0/[(2^{\sqrt{(\gamma+1)/2}})^2\gamma\beta^2]$ are the impact parameters for 90° scattering of electrons off ions or electrons off electrons. Thus $[\kappa_1(E) = \kappa_1^{ei}(E) + Z\kappa_1^{ee}(E)]$

$$\kappa_1(E) = 4\pi n_i \left(\frac{r_0}{\gamma\beta^2}\right)^2 \left[Z^2 \ln\Lambda^{ei} + \frac{4(\gamma+1)^2}{(2^{\sqrt{(\gamma+1)/2}})^4} Z \ln\Lambda^{ee}\right], \tag{9}$$

where the arguments of the Coulomb logarithm are $\Lambda^{ei} = \lambda_D/b_{\min}^{ei}$ and $\Lambda^{ee} = \lambda_D/b_{\min}^{ee}$ [30]. As these Coulomb logarithms are used in this and later calculations, they are shown in Fig. 1.

The stopping power contained in Eq. (6) consists of contributions from binary interactions with plasma electrons and from plasma oscillations. The binary contribution is [31]

$$(dE/ds)_b = -n_i Z(\gamma-1)m_0c^2 \int_{\varepsilon_{\min}}^{\varepsilon_{\max}} \varepsilon(d\sigma/d\varepsilon)d\varepsilon,$$

where the differential energy loss cross section is from Møller [23],

$$\frac{d\sigma}{d\varepsilon} = \frac{2\pi r_0^2}{(\gamma-1)\beta^2}\left(\frac{1}{\varepsilon^2} + \frac{1}{(1-\varepsilon)^2} + \left(\frac{\gamma-1}{\gamma}\right)^2 - \frac{2\gamma-1}{\gamma^2\varepsilon(1-\varepsilon)}\right), \tag{10}$$

and ε is the energy transfer in units of $(\gamma-1)m_0c^2$. The lower integration limit reflects the minimum energy transfer, which occurs when an incident electron interacts with a plasma electron at λ_D, i.e., $\varepsilon_{\min} \approx 2\gamma r_0{}^2/[\lambda_D(\gamma-1)]^2$ (unless $\gamma \to 1$, the limit for which quantum effects need to be included). The upper limit occurs for a head-on collision, for which $\varepsilon_{\max} = 0.5$.

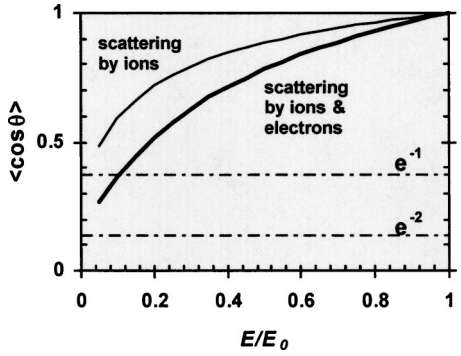

FIG. 2. The mean deflection angle $\langle\cos\theta\rangle$ is plotted against the fraction of the residual energy in a DT plasma for $e \to i$ and for $e \to i+e$ scattering (1 MeV electrons with $\rho=300$ g/cm^3, $T_e=5$ keV).

The contribution from plasma oscillations, which reflects the response of the plasma to impact parameters larger than λ_D [30], is

$$(dE/ds)_c = -4\pi r_0^2 m_0 c^2 n_i Z \beta^{-2} \ln(1.123\beta/\sqrt{2kT_e/m_0c^2}),$$

where relativistic effects are approximately included. Consequently,

$$\frac{dE}{ds} = -\frac{2\pi r_0^2 m_0 c^2 n_i Z}{\beta^2}\left[\ln\left(\frac{(\gamma-1)\lambda_D}{2\sqrt{2\gamma}r_0}\right)^2 + 1 + \frac{1}{8}\left(\frac{\gamma-1}{\gamma}\right)^2 - \left(\frac{2\gamma-1}{\gamma}\right)\ln 2 + \ln\left(\frac{1.123\beta}{\sqrt{2kT_e/m_0c^2}}\right)^2\right]. \tag{11}$$

Utilizing Eq. (11) in Eq. (6), Fig. 2 illustrates the circumstance when the incident electron ($E_0=1$ MeV) continuously changes direction as it loses energy. When $\langle\cos\theta\rangle$ equals one e-folding, $|\theta| \approx 68°$ and $E/E_0 \approx 0.1$, at which point the incident electron has lost memory of its initial direction.

Utilizing this result in Eq. (7), Fig. 3 illustrates the enhancement of dE/dx for scattering off ions and for scattering

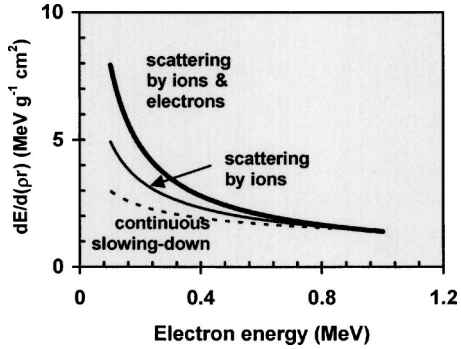

FIG. 3. Stopping power for linear energy transfer and continuous slowing down are plotted as a function of the electron energy for incident 1 MeV electrons in a DT plasma ($\rho=300$ g/cm^3, $T_e=5$ keV). Enhancement of dE/dx (solid lines) over dE/ds (dashed line) is a consequence of the effects of multiple scattering.

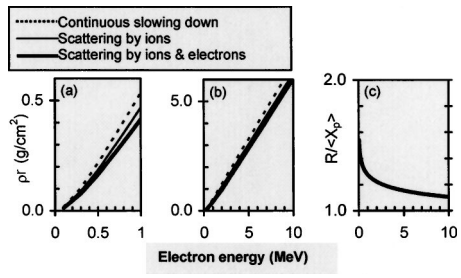

FIG. 4. The range (dashed line) and penetration for 0.1–1 MeV electrons (a) and for 1–10 MeV electrons (b) in a DT plasma ($\rho = 300$ g/cm^3, $T_e = 5$ keV). The penetration is shown for scattering off ions, and for scattering off ions plus electrons. (c) shows the ratio of range to penetration for 0.1–10 MeV electrons. As the initial electron energy decreases, the effects of multiple scattering become more pronounced, and the penetration is further diminished with respect to the range.

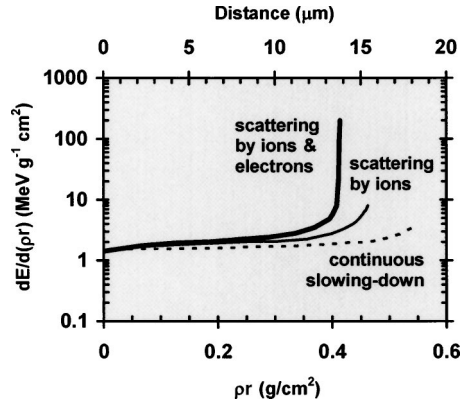

FIG. 5. The stopping power for 1 MeV electrons, plotted as a function of the electron penetration, for a DT plasma with $\rho = 300$ g/cm^3 and $T_e = 5$ keV. The three curves correspond to three different models. As a result of the scattering effects, the energy transfer increases notably near the end of the penetration (i.e., an effective Bragg peak). For these 1 MeV electrons, the effects of scattering reduce the penetration from 0.54 to 0.41 g/cm^2 [32].

off ions plus electrons. This enhancement is further illustrated in Fig. 4 where the corresponding set of curves for the range (R) and the penetration ($\langle X_p \rangle$) are shown for electrons with $E_0 = 0.1$–10 MeV. $R = \int_0^R ds' \approx \int_{E_0}^{\sim kT} (dE/ds)^{-1} dE$, and

$$\langle X_P \rangle \approx \int_{E_0}^{E_1} \langle \cos\theta \rangle \left(\frac{dE}{ds} \right)^{-1} dE, \tag{12}$$

where E_0 is the initial energy; E_1 corresponds to one e-folding of $\langle \cos\theta \rangle$ (see Fig. 2). R is the total path length the electron traverses as it scatters about and eventually thermalizes; $\langle X_p \rangle$ is the average penetration along the *initial* electron trajectory. Contributions from electron and ion scattering are shown in Fig. 4.

Three other points are worth noting: First, the temperature and density dependence are weak, i.e., a factor of 10 reduction in either temperature or density results in only ~10% reduction in the penetration. Second, as the initial electron energy decreases, the effects of scattering become more pronounced [Fig. 4(c)], an effect, very similar in nature, that is also seen in the scattering of energetic electrons in metals [33]. And third, for a given electron energy, scattering effects slightly decrease as the target plasma temperature decreases, i.e., the path of the electron slightly straightens as the target plasma temperature drops. For example, when the target plasma temperature changes from 5.0 to 0.5 keV ($\rho = 300$ g/cm^3), the ratio $R/\langle X_p \rangle$ is reduced by ~5% for 1 MeV electrons.

With the calculation of the penetration as a function of energy loss, the linear energy deposition can be evaluated (Fig. 5). In addition to the differences in total penetration with and without scattering contributions, it is seen that the linear energy transfer increases near the end of its penetration (i.e., an effective Bragg peak), an effect which is seen more weakly with just ion scattering. Such differences may need to be considered in quantitatively modeling the energy deposition of relativistic electrons for fast ignition, and for critically assessing ignition requirements [34]. It is also interesting, and a consequence of selecting 1 MeV electrons (Figs. 4 and 5), that the effects of scattering reduce the penetration from 0.54 to 0.41 g/cm^2; this latter value is close to the range of 3.5 MeV α particles, 0.3 g/cm^2, which is required for hot-spot ignition in a 10 keV plasma [3–6].

Finally, in order to explore the importance of electron-on-electron multiple scattering in a hydrogenic setting, and as definitive stopping power experiments in plasmas are extremely difficult, we propose that experiments be undertaken in which a monoenergetic electron beam, with energy between 0.1 and 1.0 MeV, scatters off thin layers of either D_2 or H_2 ice, where the thickness of the ice layer is between ~100 and 1000 μm, the appropriate thickness depending on the exact electron energy. Although there are differences in the scattering calculations for cold, condensed hydrogenic matter and a hydrogenic plasma, there is reason to believe that the *relative* importance of the electron-to-electron and the electron-to-ion multiple scattering terms will be approximately the same for both states of matter.

In summary, the energy loss and penetration of energetic electrons into a hydrogenic plasma has been analytically calculated, and the effect of scattering off ions and electrons is treated from a unified point of view. In general scattering enhances the electron linear-energy transfer along the initial electron direction, and reduces the electron penetration. Energy deposition increases near the end of its range. These results should have relevance to "fast ignition" and to fuel preheat in inertial confinement fusion, specifically to energy deposition calculations that critically assess quantitative ignition requirements.

This work was supported in part by the U.S. Department of Energy Contract No. DE-FG03-99SF21782, LLE Subcontract No. PO410025G, and LLNL Subcontract No. B313975.

[1] L. Spitzer, *Physics of Fully Ionized Gases* (Interscience, New York, 1962).
[2] B. Trubnikov, *Review of Plasma Physics 1* (Consultants Bureau, New York, 1965).
[3] S. Skupsky, Phys. Rev. A **16**, 727 (1977).
[4] C. K. Li and R. D. Petrasso, Phys. Rev. Lett. **70**, 3059 (1993).
[5] J. D. Lindl, *Inertial Confinement Fusion* (Springer, New York, 1998), and references therein.
[6] J. D. Lindl, R. L. McCrory, and E. M. Campbell, Phys. Today **45**(9), 32 (1992).
[7] R. D. Petrasso, *et al.*, Phys. Rev. Lett. **90**, 095002 (2003).
[8] M. Tabak *et al.*, Phys. Plasmas **1**, 1626 (1994).
[9] C. Deutsch *et al.*, Phys. Rev. Lett. **77**, 2483 (1996); **85**, 1140(E) (2000).
[10] S. Atzeni, Phys. Plasmas **6**, 3316 (1999).
[11] M. H. Key *et al.*, Phys. Plasmas **5**, 1966 (1998).
[12] For the case of fast ignition, numerical simulations [13] indicate that the electron transport is highly filamented due to a Weibe-like l instability [15], which occurs at early times when the beam density n_b is comparable to the critical density n_c. Plasma heating can be characterized by collective beam stopping due to coalescence of current filaments and related ion dynamics. Subsequently, however, as these electrons enter the dense plasma region where $n_e/n_b \gg 1$, the interaction can be envisioned as the linear superposition of individual, isolated electrons interacting with plasma, which is the focus of this paper.
[13] M. Honda *et al.*, Phys. Rev. Lett. **85**, 2128 (2000).
[14] M. J. Berger and S. M. Seltzer, NAS-NRC Publication No. 1133, 1965 (unpublished); these results are very close to that of the range calculation of this paper.
[15] E. S. Weibel, Phys. Rev. Lett. **2**, 83 (1959).
[16] H. H. Hubbel *et al.*, Phys. Rev. A **26**, 2460 (1982).
[17] Deutsch *et al.* have a factor of 2 error in the electron continuous-slowing-down stopping power [Eq. (3) of Ref. [9]]; in both their erratum and the original paper, this leads to about a factor of 2 overestimate in the electron range (Figs. 1(a) and 2(a) of Ref. [9] and erratum).
[18] M. D. Rosen *et al.*, Phys. Rev. A **36**, 247 (1987).
[19] B. Yaakobi *et al.*, Phys. Plasmas **7**, 3714 (2000).
[20] N. F. Mott, Proc. R. Soc. London, Ser. A **135**, 429 (1932).
[21] R. D. Evans, *The Atomic Nucleus* (McGraw-Hill, New York, 1955).
[22] Only the first term has been kept in this differential cross section. This approach is equivalent to the first-order Born approximation (the second term has an order of αZ, $\alpha = 1/137$, the fine structure constant). For heavy elements, the *e-i* cross section will need to be corrected.
[23] C. Møller, Ann. Phys. (Leipzig) **14**, 531 (1932).
[24] Since small-angle scattering dominates, we have neglected terms that are not associated with this process. Furthermore, this expression is approximately accurate only for $\gamma \lesssim 10$.
[25] *Beam and Jets in Astrophysics*, edited by P. A. Hughs (Cambridge University Press, Cambridge, England, 1991).
[26] A. Pukhov *et al.*, Phys. Plasmas **6**, 2847 (1999).
[27] H. W. Lewis, Phys. Rev. **78**, 526 (1950).
[28] S. A. Goudsmit *et al.*, Phys. Rev. **57**, 24 (1940).
[29] Since $\kappa_1(E)(dE/ds)^{-1} \propto \nu_D(E)/\nu_E(E)E$, where ν_D (ν_E) is the rate of scattering (energy loss), deflection from the initial direction is a function of the ratios of these frequencies. Furthermore, as both κ_1 and dE/ds have nearly the same dependence on $\ln \Lambda$, a consequence that it is sufficiently large (i.e., ~ 5), any sensitive dependence on the Coulomb logarithm nearly cancels out.
[30] J. D. Jackson, *Classical Electrodynamics* (Wiley, New York, 1975).
[31] E. Rohrlich *et al.*, Phys. Rev. **93**, 38 (1954).
[32] In Deutsch *et al.*, their penetration is about four times smaller than their range for 1 MeV electrons [Figs. 1(a) and 2(a) of Ref. [9] and erratum]. Even including electron scattering effects, the results of the present paper indicate a penetration that is only a factor of 1.32 smaller than the range of 1 MeV electrons. As best we can tell, the approach of Deutsch *et al.* is unjustified since they invoke an approximation by P. C. Hemmer and I. E. Farquhar [Phys. Rev. **168**, 294 (1968); see Eq. (67) and discussion], which is valid only for small angle deflections and for small energy loss. This approximation is invalid in the present context of large deflections and total energy loss.
[33] K. H. Weber, Nucl. Instrum. Methods **25**, 261 (1964).
[34] Whether considering fast ignition or electron preheat, the distribution of electron energies about their mean will smear out the energy deposition, making it more uniform.

To be published in **Phys. Rev.** E, 73, January 2006.

Stopping, Straggling, and Blooming of Directed Energetic Electrons in Hydrogenic and Arbitrary-Z Plasmas

C. K. Li and R. D. Petrasso*
Plasma Science and Fusion Center, Massachusetts Institute of Technology, Cambridge, MA 02139

From fundamental principles, the interaction of directed energetic electrons with hydrogenic and arbitrary-Z plasmas is analytically modeled. For the first time the effects of stopping, straggling, and beam blooming, a consequence of scattering and energy loss, are rigorously treated from a unified approach. Enhanced energy deposition occurs in the latter portion of the penetration and is inextricably linked to straggling and blooming. These effects, which have a strong Z dependence, will be important for evaluating the requirements of fast ignition and tolerable levels of electron preheat.

PACs No. 52.55.Pi, 52.40.Mj, 52.50.Gj, 52.25.Tx

A basic problem in plasma physics is the interaction and energy loss of energetic charged particles in plasmas [1-3], including the effects of penetration, longitudinal straggling, and lateral blooming. This problem has traditionally focused on ions (*i.e.* protons, α's, etc.), either in the context of heating and/or ignition in, for example, inertially confined plasmas (ICF) [3-7]; or the use of these particles for diagnosing implosion dynamics [8]. More recently, prompted in part by the concept of fast ignition (FI) for ICF [9], workers have begun considering energy deposition from relativistic electrons in deuterium-tritium (DT) plasmas [9-14]. In this context, we recently calculated the mean penetration and stopping power for energetic electrons interacting with a uniform hydrogenic plasma of arbitrary density and temperature. Therein the randomizing effect of electron scattering, which has a cumulative effect of bending the path of the electrons away from their initial direction, was linked to energy loss [14]. In this Letter we present calculations which show, for the first time, the effects of longitudinal straggling and transverse blooming, and their inextricable relationship with enhanced electron energy deposition. We demonstrate that, while the initial penetration results in approximate uniform energy deposition, the latter penetration has mutual couplings of energy loss, straggling, and blooming that lead to an extended region of enhanced, non-uniform energy deposition. This present work is important for quantitatively evaluating the energy deposition in several current problems. In the case of FI, for example, there have been no evaluations which have treated either straggling or blooming upon the energy deposition, without which there can be no confident assessment of ignition requirements. The calculations herein therefore form the foundation for a baseline, at the very least, or an accurate assessment, at the very most, by which to evaluate these effects upon FI. In addition to FI, these calculations are sufficiently general to be of relevance to other current problems, such as fast electron preheat [15] in ICF, or to energy deposition and penetration of relativistic electrons in astrophysical jets [16].

To delineate these processes, we calculate the different moments by analytically solving an integro-differential diffusion equation [17], thereby determining the angular and spatial distributions of the scattered electrons.

$$\frac{\partial f}{\partial s} + \mathbf{v} \cdot \nabla f = n_i \int \left[f(\mathbf{x}, \mathbf{v}', s) - f(\mathbf{x}, \mathbf{v}, s) \right] \sigma\left(|\mathbf{v} - \mathbf{v}'| \right) d\mathbf{v}' , \tag{1}$$

where $f(\mathbf{x}, \mathbf{v}, s)$ is the distribution function; n_i is the number density of fully ionized plasma ions of charge Z; $\mathbf{x}$ is the position where scattering occurs; $\sigma=\sigma_{ei}+Z\sigma_{ee}$ is the total scattering cross section with σ_{ei} the Rutherford *e-ion* cross section [18], and σ_{ee} the Møller *e-e* cross section [19]. We solve this equation in cylindrical coordinates with the assumption that the scattering is azimuthally symmetric. After expanding the distribution in spherical harmonics and substituting into Eq. (1), two differential equations for the longitudinal and lateral distributions are obtained. For the longitudinal distribution:

$$\frac{\partial F^n_{\ell m}(s)}{\partial s} + \kappa_\ell(s) F^n_{\ell m}(s) - n\left[\frac{\ell}{\sqrt{4\ell^2 - 1}} F^{n-1}_{\ell-1,m}(s) + \frac{\ell+1}{\sqrt{4(\ell+1)^2 - 1}} F^{n-1}_{\ell+1,m}(s) \right] = 0 . \tag{2}$$

And for lateral distribution:

$$\frac{\partial F^n_{\ell m}(s)}{\partial s} + \kappa_\ell(s) F^n_{\ell m}(s) - \frac{n}{2}\left[\sqrt{\frac{(\ell+m)(\ell+m-1)}{4\ell^2 - 1}} F^{n-1}_{\ell-1,m-1}(s) + \sqrt{\frac{(\ell+m+2)(\ell+m+1)}{4(\ell+1)^2 - 1}} F^{n-1}_{\ell+1,m+1}(s) \right.$$
$$\left. - \sqrt{\frac{(\ell-m)(\ell-m-1)}{4\ell^2 - 1}} F^{n-1}_{\ell-1,m+1}(s) - \sqrt{\frac{(\ell-m+2)(\ell-m+1)}{4(\ell+1)^2 - 1}} F^{n-1}_{\ell+1,m+1}(s) \right] = 0 , \tag{3}$$

where the moments are defined as $F^n_{\ell m}(s) = \int_{-\infty}^{\infty} x_j^n f_{\ell m}(\mathbf{x}, s) d\mathbf{x}$, and j =1,2,3 represents x, y, z, respectively.

$$\kappa_\ell(s) = n_i \int \left(\frac{d\sigma}{d\Omega} \right) [1 - P_\ell(\cos\theta)] d\Omega , \tag{4}$$

where $(d\sigma/d\Omega)$ is the differential cross section of either *e-ion* or *e-e* scattering [18,19,14], $P_\ell(\cos\theta)$ are the Legendre polynomials, and $\kappa_\ell(s)$ are directly related to the basic transport cross sections [2]. Equations (2) and (3) are coupled to adjacent orders in n, and are solved with the boundary condition $F^n_{\ell m}(s) = \sqrt{(2\ell+1)/4\pi}\,\delta_{m0}\delta_{n0} \exp\left(- \int_0^S \kappa_\ell(s') ds' \right)$, where $F^n_{\ell m}(0) = 0$ for $n \neq 0$. Solving for κ_1 and κ_2

$$\kappa_1 = 4\pi n_i \left(\frac{r_0}{\gamma\beta^2} \right)^2 \left[Z^2 \ln\Lambda^{ei} + \frac{4(\gamma+1)^2}{\left(2^{\sqrt{(\gamma+1)/2}}\right)^4} Z \ln\Lambda^{ee} \right] ; \tag{5}$$

and

$$\kappa_2 = 12\pi n_i \left(\frac{r_0}{\gamma\beta^2} \right)^2 \left[Z^2 \left(\ln\Lambda^{ei} - \frac{1}{2} \right) + \frac{4(\gamma+1)^2}{\left(2^{\sqrt{(\gamma+1)/2}}\right)^4} Z \left(\ln\Lambda^{ee} - \frac{1}{2} \right) \right] . \tag{6}$$

κ_1 is related to the slowing-down cross section [2], which characterizes the loss of directed velocity in the scattering; and κ_2 is related to the deflection cross section which represents

the mean-square increment in the transverse electron velocity during the scattering process [2]. β = v/c and $\gamma = (1-\beta^2)^{-1/2}$; $r_0 = e^2/m_0c^2$ is the classical electron radius. The arguments of the Coulomb logarithm are: $\Lambda^{ei} = \lambda_D / b^{ei}_{\min}$, and $\Lambda^{ee} = \lambda_D / b^{ee}_{\min}$, where λ_D is the Debye length, and $b^{ei}_{\min}$ ($b^{ee}_{\min}$) is the larger of b^{ei}_q (b^{ee}_q) and $b^{ei}_\perp$ ($b^{ee}_\perp$) [14]. b^{ei}_q and b^{ei}_q are approximately the electron deBroglie wavelength, and $b^{ei}_\perp = Zr_0/\gamma\beta^2$ and $b^{ee}_\perp \approx 2(\gamma+1)r_0/[(2^{\sqrt{(\gamma+1)/2}})^2\gamma\beta^2]$ are the impact parameters for 90° scattering of electrons off ions or electrons off electrons [14]. The angular distribution function is obtained

$$f(\theta,E) = \frac{1}{4\pi}\sum_{\ell=0}^{\infty}(2\ell+1)P_\ell(\cos\theta)\exp\left(-\int_{E_0}^{E}\kappa_\ell\left(E^{'}\right)\left(\frac{dE^{'}}{ds}\right)^{-1}dE'\right), \tag{7}$$

from which $\langle P_\ell(\cos\theta)\rangle$ is calculated

$$\langle P_\ell(\cos\theta)\rangle = \exp\left\{-\int_{E_0}^{E}\kappa_\ell(E^{'})\left(\frac{dE'}{ds}\right)^{-1}dE'\right\}; \tag{8}$$

where *dE/ds* is plasma stopping power taken from Ref. [14],

$$\frac{dE}{ds} = -\frac{2\pi r_0^2 m_0c^2 n_i Z}{\beta^2}\left[\ln\left(\frac{(\gamma-1)\lambda_D}{2\sqrt{2\gamma}r_0}\right)^2 + 1 + \frac{1}{8}\left(\frac{\gamma-1}{\gamma}\right)^2 - \left(\frac{2\gamma-1}{\gamma}\right)\ln 2 + \ln\left(\frac{1.123\beta}{\sqrt{2kT_e/m_0c^2}}\right)^2\right], \tag{9}$$

which consists of contributions from binary interactions with plasma electrons and from plasma oscillations. From these results, we solve Eqs. (2) and (3), and evaluate basic moments required for the calculation of the longitudinal and lateral distributions:

$$\langle x\rangle = \int_{E_0}^{E}\langle P_1(\cos\theta)\rangle\left(\frac{dE^{'}}{ds}\right)^{-1}dE^{'}, \tag{10}$$

which was evaluated in previous work for the case of 1-MeV electron stopping in a DT 300 g /cm^3 plasma at 5 keV. This results in a penetration (<x>) of 13.9 μm [14]. However, for astrophysical jets, for which $n_e \sim 10/\text{cm}^3$, the penetration is ~ 10^4 light years.

$$\langle x^2\rangle = \frac{2}{3}\int_{E_0}^{E}\langle P_1(\cos\theta)\rangle\left(\frac{dE^{'}}{ds}\right)^{-1}\left(\int_{E_0}^{E'}\frac{1+2\langle P_2(\cos\theta)\rangle}{\langle P_1(\cos\theta)\rangle}\left(\frac{dE^{"}}{ds}\right)^{-1}dE^{"}\right)dE^{'}, \tag{11}$$

Because of azimuthally symmetry, $\langle y\rangle = \langle z\rangle = 0$, and

$$\langle y^2\rangle = \langle z^2\rangle = \frac{2}{3}\int_{E_0}^{E}\langle P_1(\cos\theta)\rangle\left(\frac{dE^{'}}{ds}\right)^{-1}\left(\int_{E_0}^{E'}\frac{1-\langle P_2(\cos\theta)\rangle}{\langle P_1(\cos\theta)\rangle}\left(\frac{dE^{"}}{ds}\right)^{-1}dE^{"}\right)dE^{'}. \tag{12}$$

In evaluating Eqs. (10), (11) and (12), one needs to evaluate $\langle P_1(\cos\theta)\rangle$ and $\langle P_2(\cos\theta)\rangle$, the first and second order mean Legendre polynomials. Substituting Eqs. (5) or (6), respectively, into Eq. (8), and using the stopping power [Eq. (9)], both quantities are readily calculated.

Range straggling is defined by

$$\Sigma_R(\text{E}) = \sqrt{\langle x^2\rangle - \langle x\rangle^2}. \tag{13}$$

Beam blooming is defined by

$$\Sigma_B(E) = \sqrt{\langle y^2 \rangle}\ . \tag{14}$$

Both Σ_R and Σ_B are evaluated numerically using Eqs. (10), (11), and (12). Although the focus of this Letter is on hydrogenic plasmas (Z=1), the strong Z–dependence of scattering is directly reflected in the penetration, straggling and blooming (Table 1). In particular, with increasing Z the penetration $\langle x \rangle$, but not the total path length ($R = \int_{E_0}^{\sim T_e} \left(dE/ds\right)^{-1} dE$), rapidly drops and blooming effects ($\Sigma_B/\langle x \rangle$) notably increase. (The constancy in R is a result of the fixed n_e used for the calculations of Table 1.) Figure 1 illustrates further details of Σ_R and Σ_B as 1-MeV electrons slow in a DT plasma, which demonstrates the importance of these effects as the electron energy degrades. As a consequence, an extended region of energy deposition occurs longitudinally (± ~3 μm) and laterally (± ~5 μm) about the mean penetration, 13.9 μm for this case.

Z	ρ (g/cm^3)	R (μm)	$\langle x \rangle$ (μm)	ρ$\langle x \rangle$ (g/cm^2)	Σ_R (μm)	Σ_B (μm)	$\frac{\Sigma_R}{\langle x \rangle}$	$\frac{\Sigma_B}{\langle x \rangle}$
1	300	17.9	13.9	0.42	2.7	4.7	0.19	0.33
4	271	17.9	10.6	0.29	3.8	5.4	0.36	0.51
13	249	17.9	6.3	0.16	4.2	5.1	0.67	0.81
29	265	17.9	3.7	0.10	3.7	4.2	1.0	1.14

TABLE 1. Interactions of 1 MeV electrons with DT, beryllium, aluminum and copper plasmas, assuming plasma T_e= 5 keV and n_e=7.2×10^{25} in every cases. For Cu plasma, bremsstrahlung loses are about 5%, and are ignored.

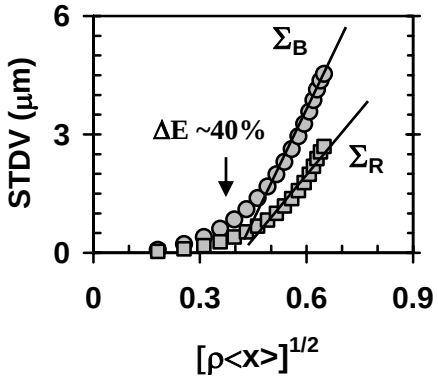

FIG. 1. Σ_R and Σ_B are plotted as a function of square root of the penetration for a 1-MeV electron beam in a DT plasma of 300g/cm^3 at 5 keV. When the electrons have lost more than ~40% of their initial energy, both Σ_R and Σ_B are approximately proportional to $\sqrt{\rho\langle x \rangle}$.

From a different point of view, Figure 2 shows the effective enhancement of the stopping power in the extended region in which straggling and blooming are important. The combined effects of Σ_R and Σ_B will result in an asymmetric energy deposition region about the mean penetration. In contrast to earlier work [10] these calculations inextricably link energy loss, straggling, and blooming. Thus the assumption of uniform energy deposition over the entire path length of the electron's trajectory [11] has only approximate justification.

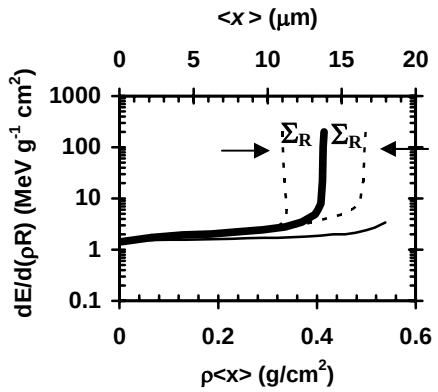

FIG. 2. The stopping power is plotted as a function of the electron penetration for 1-MeV electrons in a DT plasma (ρ=300g/cm^3 and T_e=5 keV). The heavy solid line represents the mean energy loss, while the two dashed lines indicate the straggling range over which energy is effectively spread. (In this plot, important contributions from blooming are not included; see text) The thin line illustrates the continuous slowing-down approximation [14], and is directly related to *R*, the total path length.

The insensitivity of scattering effects ($\Sigma_R/\langle x\rangle$ and $\Sigma_B/\langle x\rangle$) and $\rho\langle x\rangle$ upon ρ is illustrated in Table 2. This shows that density gradients, such as would occur towards the core region of an actual FI experiment, will not impact the general scope of these calculations. The slight increase in $\rho\langle x\rangle$ with ρ simply reflects the slight decrease in Coulomb logarithm of the stopping power [Eq. (9)] as ρ increases. Furthermore, these results are quite insensitive over a wide range in temperature [14].

ρ (g/cm^3)	$\langle x\rangle$ (μm)	$\rho\langle x\rangle$ (g/cm^2)	Σ_R (μm)	Σ_B (μm)	$\frac{\Sigma_R}{\langle x\rangle}$	$\frac{\Sigma_B}{\langle x\rangle}$
100	39.7	0.40	8.0	13.4	0.20	0.34
300	13.9	0.42	2.7	4.7	0.19	0.33
1000	4.5	0.45	0.9	1.5	0.20	0.33

TABLE 2. Interactions of 1 MeV electrons with DT plasmas of various densities.

E_0	ΔE	$\langle x \rangle$	$\rho\langle x \rangle$	Σ_R	Σ_B	$\frac{\Sigma_R}{\langle x \rangle}$	$\frac{\Sigma_B}{\langle x \rangle}$
(MeV)	(%)	(μm)	(g/cm^2)	(μm)	(μm)		
0.1	25	0.45	0.013	0.12	0.17	0.27	0.38
1.0	40	13.9	0.42	2.7	4.7	0.19	0.33
5.0	50	94.1	2.82	10.8	20.8	0.12	0.22
10	65	201	6.04	15.7	33.2	0.08	0.17

TABLE 3. Interactions of 0.1-10 MeV electrons with DT plasma of 300g/cm^3. ΔE is the percentage of energy loss when Σ_R and Σ_B are starting to become significant, as illustrated in Fig. 1.

E_0		ρ	R	$\langle x \rangle$	$\rho\langle x \rangle$	Σ_R	Σ_B	$\frac{\Sigma_R}{\langle x \rangle}$	$\frac{\Sigma_B}{\langle x \rangle}$
(keV)		(g/cm^3)	(μm)	(μm)	(g/cm^2)	(μm)	(μm)		
10	DT	0.25	6.0	4.72	1.2×10^{-4}	1.09	1.60	0.23	0.33
		1.0	1.67	1.35	1.4×10^{-4}	0.31	0.44	0.23	0.32
	Be	1.85	0.84	0.57	1.1×10^{-4}	0.18	0.24	0.31	0.42
		7.4	0.23	0.16	1.2×10^{-4}	0.05	0.067	0.31	0.42
	CH	1.0	1.16	0.72	7.2×10^{-5}	0.26	0.35	0.36	0.48
		4.0	0.32	0.21	8.4×10^{-5}	0.076	0.10	0.36	0.48
100	DT	0.25	330	283	7.1×10^{-3}	42.8	75.4	0.15	0.27
		1.0	86.0	75.0	7.5×10^{-3}	11.1	19.1	0.15	0.26
	Be	1.85	43.0	31.0	5.7×10^{-3}	8.17	12.1	0.26	0.39
		7.4	11.3	8.5	6.2×10^{-3}	2.20	3.27	0.26	0.38
	CH	1.0	59.7	42.4	4.2×10^{-3}	13.6	17.2	0.32	0.41
		4.0	15.6	11.0	4.4×10^{-3}	3.57	4.49	0.32	0.41

TABLE 4. Interactions of 10-keV and 100-keV electrons with DT, Be and plastic CH plasmas, common ablator or fuel materials of ICF. The plasma T_e ~10eV. (For CH, the scattering effects are calculated for carbon ions and all plasma electrons).

Table 3 illustrates the enhancement of scattering effects ($\Sigma_R/\langle x \rangle$ and $\Sigma_B/\langle x \rangle$) as the electron energy decreases from 10 to 0.1 MeV. These effects are also important for the electron preheat problem [14], as shown in Tables 4, but for regimes of lower energy (10 to 100 keV) and much lower density. Similar to Table 1, $\Sigma_R/\langle x \rangle$ and $\Sigma_B/\langle x \rangle$ are seen to increase with the Z of the plasma, where the selected materials are common to those used, or contemplated for use at either OMEGA or the National Ignition Facility (NIF), for ablators and/or the fuel [4]. Focusing on the NIF, and direct drive scenarios, the DT ice thickness for the capsule is approximately 300 μm, which is very comparable to the penetration of 100

keV electrons. For present NIF indirect drive scenarios, the Be ablator of the capsule is ~ 150 μm thick, which is ~ 5 times larger than the penetration of 100 keV electrons. Finally the density jump assumed in the Tables (≈4) could, for example, reflect the effects of the passage of a strong shock. As illustrated in Table 2 for very different conditions, $\rho\langle x\rangle$ is again insensitive to the change in ρ, but $\langle x\rangle$ is notably affected.

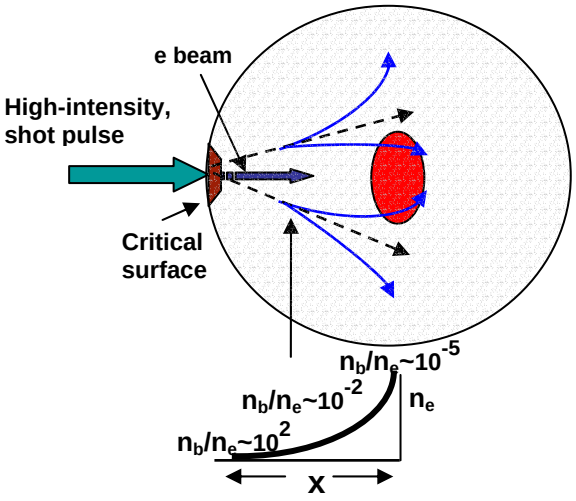

FIG. 3. Schematic illustration of beam blooming in a pre-compressed FI capsule. Two distinct regions for electron transport are illustrated: First, when $n_b/n_e > 10^{-2}$, the electron transport is highly filamented due to Weibel-like instabilities which dominate energy loss and beam blooming; however, for $n_b/n_e < 10^{-2}$, for which λ_D is clearly smaller than the energetic electron gyro radius associated with the beam current, the Weibel-like instabilities are stabilized and the electrons are then subject to the scattering, straggling, and blooming processes described herein. The dashed lines schematically indicate electron beam trajectories without the effects of blooming and straggling (see text).

Figure 3 shows a schematic representation of FI capsule. The relativistic electrons are generated by an intense laser interacting at the critical surface. As the electrons are initially transported, they are subject to Weibel-like instabilities [20,21] which can cause both spreading and energy loss in this region. However, for electrons that transport farther into the increased density portions of the capsule ($n_b/n_e < 10^{-2}$), Weibel-like instabilities are stabilized and the electrons then become subject to the scattering processes described herein. This stabilization can be understood since the gyro radius associated with the self-generated fields of the beam current is much larger than λ_D . This indicates the dominance of the binary interactions, and the motivation for exploring these processes in this paper. Thus in this regime, the interaction can be envisioned as the linear superposition of individual, isolated electrons interacting with plasma. Hence these scattering processes, which involve energy loss, straggling and beam blooming become the ultimate mechanism that determines the details of energy deposition, whether in the dense core or outside, and therefore ultimately determine the effectiveness of capsule ignition. From a different point of view, the extent of

beam blooming and straggling is critical for FI target design since the finite size of the highly compressed core requires accurate understanding and control of beam divergence which, if too severe, will preclude ignition.

In summary, from fundamental principles the interaction of directed energetic electrons with hydrogenic and arbitrary-Z plasmas is analytically modeled. For the first time, the effects of stopping, straggling, and beam blooming, a consequence of multiple scattering and energy loss, are rigorously treated from a unified approach. The sensitivity of these scattering effects, or the lack thereof, has been illustrated for several cases of different Z, densities, and initial electron energies, all of which span the range of relevance to many present and planned experiments. For Fast Ignition or electron preheat, enhanced energy deposition is found to be inextricably linked to beam blooming and straggling. These effects will therefore be important for evaluating the requirements of fast ignition and tolerable levels of electron preheat.

This work was supported in part by U.S. Department of Energy Contract #DE-FG03-99SF21782, LLE subcontract #PO410025G, LLNL subcontract #B313975, and the Fusion Science Center for Extreme States of Matter and Fast Ignition Physics at University of Rochester.

* Also Visiting Senior Scientist at LLE, Univ. Rochester.

[1] L. Spitzer, *Physics of Fully Ionized Gases* (Interscience, New York, 1962).
[2] B. Trubnikov, *Review of Plasma Physics* 1 (consultants Bureau, New York, 1965).
[3] C. K. Li and R. D. Petrasso, Phys. Rev. Lett. **70**, 3063 (1993).
[4] J. D. Lindl, *Inertial Confinement Fusion* (Springer-Verlag, New York, 1998).
[5] J. D. Lindl, R. L. McCrory, and E. M. Campbell, Phys. Today, **45**, 32 (1992).
[6] S. Skupsky, Phys. Rev. **16**, 727 (1977);
[7] C. K. Li and R. D. Petrasso, Phys. Rev. Lett. **70**, 3059 (1993).
[8] R. D. Petrasso *et al*., Phys. Rev. Lett. **90**, 095002 (2003).
[9] M. Tabak *et al.,* Phys. Plasmas **1**, 1626 (1994).
[10] C. Deutsch, *et al*., Phys. Rev. Lett. **77**, 2483 (1996).
[11] S. Atzeni, Phys. Plasmas **6**, 3316 (1999).
[12] M. H. Key *et al*., Phys. Plasmas **5**, 1966 (1998).
[13] C. Ren *et al*., Phys. Rev. Lett. **93,** 185004 (2004).
[14] C. K. Li and R. D. Petrasso, Phys. Rev. E **70**, 067401 (2004).
[15] M. D. Rosen *et al.,* Phys. Rev. A **36**, 247 (1987).
[16] *Beam and Jets in Astrophysics*, edited by P. A. Hughs (Cambridge Univ. Press, 1991)
[17] H. W. Lewis, Phys. Rev. **78**, 526 (1950).
[18] N. F. Mott, Proc. R. Soc. **A135**, 429 (1932).
[19] C. Møller, Ann. Physik (Leipz) **14**, 531 (1932).
[20] E. S. Weibel, Phys. Rev. Lett. **2**, 83 (1959).
[21] M. Honda *et al*., Phys. Rev. Lett. **85,** 2128 (2000).

To be published in ***Physics of Plasmas***

(Subject to minor revision)

Energy deposition of MeV electrons in compressed targets of fast-ignition inertial confinement fusion

C. K. Li and R. D. Petrasso

Plasma Science and Fusion Center, Massachusetts Institute of Technology,

Cambridge, MA 02139

ABSTRACT

Energy deposition of MeV electrons in dense plasmas, critical for fast ignition in inertial confinement fusion (ICF), is modeled analytically. It is shown that classical stopping and scattering dominate electron transport and energy deposition when the electrons reach the dense plasmas in the cores of compressed targets, while "anomalous" stopping associated with self-generated fields and micro instabilities (suggested by previous simulations) might initially play an important role in the lower-density plasmas outside the dense core. For MeV electrons in pre-compressed deuterium-tritium (DT) fast-ignition targets, while the initial penetration results in approximately uniform energy deposition, the latter stages involve mutual couplings of energy loss, straggling, and blooming that lead to enhanced, non-uniform energy deposition. This model can be used for quantitatively assessing ignition requirements for fast ignition.

I. INTRODUCTION

Fast ignition,[1] an alternative approach to inertial confinement fusion (ICF), has recently attracted significant attention. In this scheme, different from the conventional approach to central hot-spot ignition, a pre-compressed deuterium-tritium (DT) target will be ignited by an external "spark". Since it separates capsule compression from hot spot formation, fast ignition may potentially relax the conditions on target compression and reduce the total energy requirements for ICF ignition, leading to higher target gain.[1-3]

Successful realization of fast ignition requires understanding and controlling of the transport and energy deposition of MeV electrons in the target. Energetic electrons are generated by an ultrahigh-intensity ($\sim 10^{20}$ W/cm^2), short-pulse (~10 ps) laser interacting at the critical surface of a pre-compressed target. During a time period of ~10 ps, a total energy ~ 10 kJ needs to be delivered to the compressed core; fast ignition then occurs in response to electron energy deposition, with DT alphas bootstrapping a fusion burn wave that propagates to the surrounding dense fuel. [1-3]

As illustrated schematically in Fig. 1, the generated electron beam is typically characterized by a radius ~10 μm and current $\geq 3\times10^8$ A. As it propagates over a distance ~ 100 μm to the core, such an electron beam experiences a tremendous dynamic range of plasma conditions, from the initial critical surface ($n_c \sim 10^{21}/\text{cm}^3$) to the highly compressed core ($n_e \sim 10^{26}/\text{cm}^3$). Return currents and associated self fields are generated.[1-3] Numerical simulations [4-6] suggest that the electron transport is highly filamented due to self fields and microscopic instabilities,[7] which occur at early times when beam density, n_b, is comparable to or larger than the critical density n_c. In these simulations plasma heating is dominated by "anomalous" stopping which may be largely characterized by collective beam stopping, possibly due to coalescence of current filaments and related ion dynamics. Return-current Ohmic heating also plays an important role due to the relatively low plasma temperature.[3] Subsequently, however, as these electrons enter the dense plasma region where $n_b/n_e << 1$ and plasma $T_e \sim$ keV, classical Coulomb collisions will dominate electron transport and energy deposition (as will be discussed in the next section).

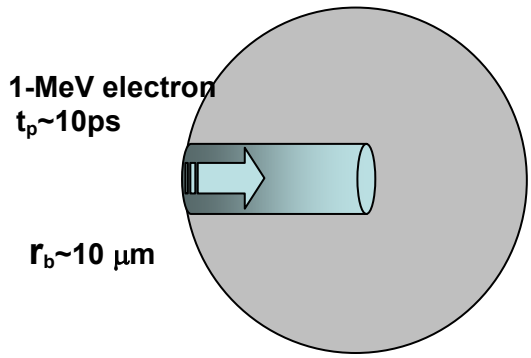

FIG. 1. The fast ignition scheme is schematically illustrated in this diagram: ~MeV electrons generated by high intensity, shot-pulse laser at the critical surface need to transport to the pre-compressed target core. These electrons interact with, and deposit energy to, the background plasma whose density evolves from 10^{21} to 10^{26} /cm^3. Typically, the electron beam has a pulse length ~10 ps and beam radius ~10 μm.

This paper is organized as follows. Section II discusses interaction regimes for MeV electrons in dense plasmas. An analytic model, which links electron energy loss with range straggling and beam blooming, is presented in Section III. Section IV discusses some fundamental dependences and consequences of these calculations, while Section V summarizes our major results.

II. ELECTRON TRANSPORT AND ENERGY DEPOSITION IN THE DENSE CORE

While numerical simulations have suggested that microscopic instabilities and anomalous stopping might initially play an important role in the outer region of low-density plasma, we argue that the interaction of the electrons with dense plasma in the

core is dominated by classical Coulomb collisions and that the effects of scattering will ultimately determine the electron transport and energy deposition. To illustrate this, we consider a 1-MeV electron beam (beam radius r_b=10 μm) in a compressed DT target (ρ=300 g/cm^3 and T_e=5 keV). The maximum field $B_{max}= \mu_0 I_b/(2\pi r_b)$ occurs at the beam surface, where

$$I_b = n_b e v \pi r_b^2 = \frac{\varepsilon_b(\mathrm{kJ})}{E(\mathrm{MeV}) t_b(\mathrm{ps})} \times 10^9 (\mathrm{Amp}) \qquad (1)$$

is the beam current calculated in terms of electron energy E, beam energy ε_b, and the beam pulse duration t_b.

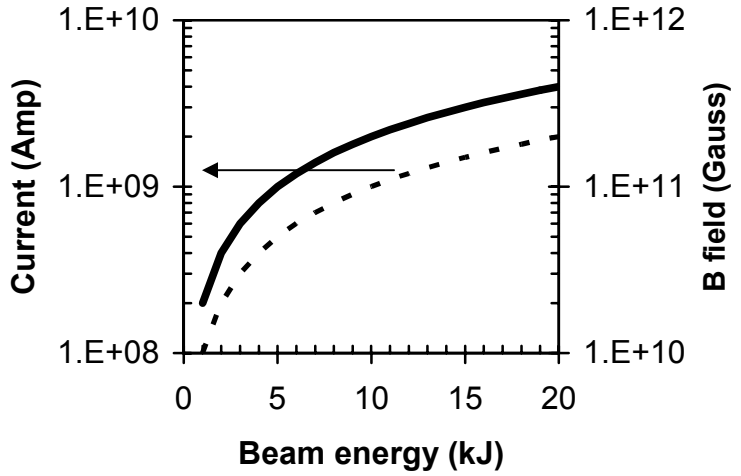

FIG. 2. The beam current I_b and associated B_{max} are plotted as a function of the beam energy ε_b, for E=1 MeV and t_b =10 ps, a typical case relevant to fast ignition.

Relevant to fast ignition (E=1 MeV and t_b =10 ps), Fig. 2 plots the I_b and associated B_{max} as a function of the beam energy. For example, for ignition energy ε_b=15 kJ, $I_b \sim 10^9$ A and $B_{max} \sim 10^{11}$ Gauss are expected. The maximum electron gyro radius (r_g) associated to B_{max} is $r_g(\mathrm{cm}) = v m_e c/eB = 2.38\times10^3 \sqrt{E(\mathrm{MeV})}/B(\mathrm{Gauss})$. Figure 3 shows r_g as a function of beam energy for different beam radii; it is consistently larger than plasma Debye length λ_D. This suggests that an electron does not feel the magnetic field locally but is subjected to Coulomb collisions. In addition, while $\omega_{ce}\tau$ >>1 in this region, one has $L_{||} >> \lambda$ and $L_\perp >> \sqrt{\lambda r_g}$ (ω_{ce} is the electron gyro frequency; λ=vτ is the mean free path and τ is the collision time; $L_{||}$ is the longitudinal plasma scale length and $L_\perp$ lateral scale length). This is the typical collisional transport regime. [10-12] Furthermore, as is illustrated in Fig. 4, the resistivity of a compressed core is shown to be very small[13] due to the relative high plasma temperature [10] resulting from shock heating and capsule compression. For a typical case of fast ignition, the density of return current j~10^{14} A/cm^2 (which is approximately equal to the forward current density) and electron penetration <x> ~10 μm (ρ=300g/cm$_3$ and Te = 5 keV), the resistivity (η~10^{-7} Ωcm) would lead the heating intensity <x>ηj^2 ~10^{18} W/cm^2, which is much smaller than the intensity for an

ignition[2] (I_{ig} =2.4×10^{19} ×(300g cm^{-3}/100g cm^{-3})$^{0.95}$ ~ 7.6×10^{19} W/cm^2. This clearly suggests that Joule heating is not a major mechanism for heating the core plasmas although this does not necessarily mean that it is completely negligible. Consequently, the interaction of the electron with dense plasma is well characterized by classical Coulomb collisions and the effects of the scattering will dominate the electron transport and energy deposition.

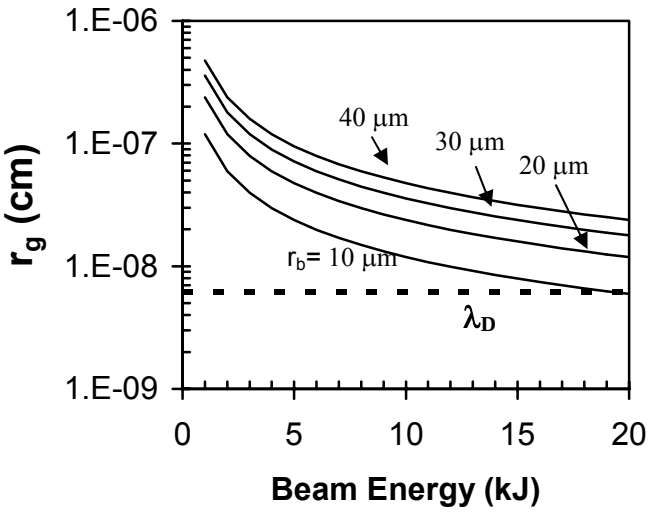

FIG. 3. The maximum electron gyroradius r_g as a function of beam energy for the cases where beam radius r_b=10, 20, 30, 40 μm, and the plasma Debye length λ_D in the compressed target (a DT plasma with ρ=300 g/cm^3 and T_e=5 keV). It is seen that for the cases we are considering r_g's are all consistently larger than the λ_D. Only for very large energy deposition and very small deposition regions does r_g approach λ_D.

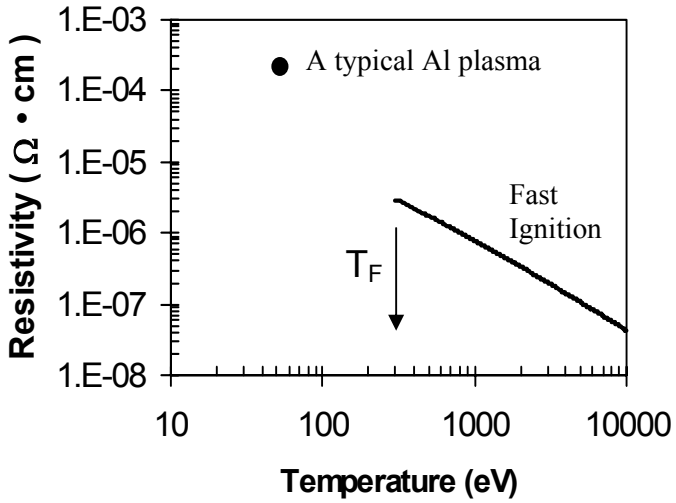

FIG. 4. The resistivity of a compressed core is shown to be several orders of magnitude smaller than that of a plasma generated by a short pulse laser on a solid target such as Al (for which case the resistivity plays an important role in plasma heating).[13]

Thus a criterion for distinguishing the interaction regimes and for illustrating their relative importance is approximately established based on above physics arguments as

$$\zeta \equiv \left.\frac{n_b}{n_e}\right|_{r_g=\lambda_D} = \frac{4\pi^2 t_b \sqrt{2m_e E^3}}{\mu_0^2 r_0 T_e \varepsilon_b} \ , \tag{2}$$

where r_0 is the classic electron radius. Figure 5 shows this ratio as a function of the beam energy for the case of 1 MeV electrons with t_b=10 ps in a DT plasma at 5 keV: when $n_b/n_e \geq \zeta$ the effects of self fields and associated instabilities are important, while when $n_b/n_e < \zeta$ the effects of classical Coulomb scattering are dominant.

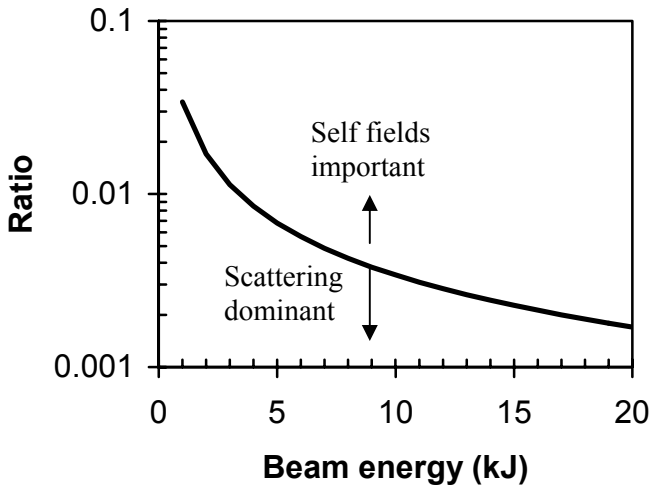

FIG. 5. The ratio defined by Eq. (2) is plotted as a function of the beam energy for the case of 1-MeV electrons with t_b=10 ps in plasma at 5 keV: when $n_b/n_e \geq \zeta$ the effects of self fields and associated instabilities are important while when $n_b/n_e < \zeta$ the effects of classical Coulomb scattering are dominant. It is the later that the ignition occurs and the ignition conditions are determined.

We summarize and restate the above discussions from a different point of view in Fig. 6: when energetic electrons travel farther into the rapidly increased density portions of the capsule ($n_b/n_e < 10^{-2}$), Weibel-like instabilities[7] are stabilized and the electrons are subject primarily to scattering processes. This stabilization can be understood since the gyro radius associated with the self-generated fields of the beam current is much larger than λ_D . Thus in this regime, the interaction can be envisioned as the linear superposition of individual, isolated electrons interacting with plasma. Hence these scattering processes, which involve energy loss, straggling and beam blooming, become the dominant mechanism that determines the details of energy deposition, whether in the dense core or outside, and therefore ultimately determine the effectiveness of capsule ignition.

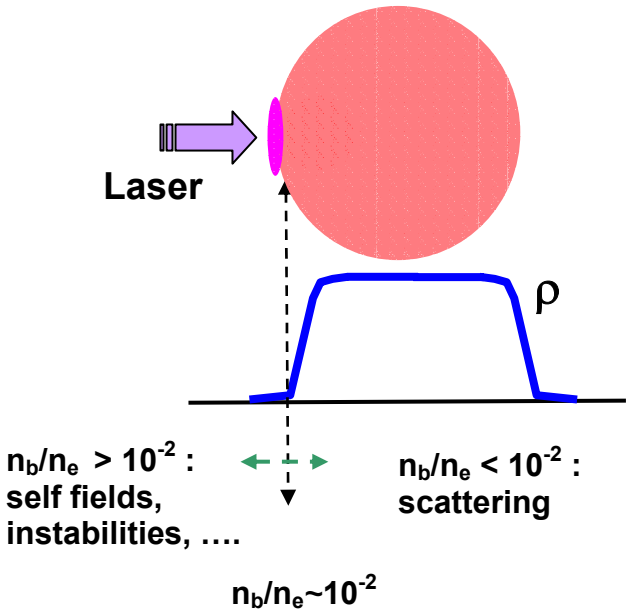

FIG. 6. Schematic illustration of MeV electron transport and energy deposition in a pre-compressed target. Two distinct regions for electron transport are illustrated: First, when $n_b/n_e > 10^{-2}$, electron transport is highly filamented due to Weibel-like instabilities which dominate energy loss and beam blooming; however, for $n_b/n_e < 10^{-2}$, for which λ_D is clearly smaller than the energetic electron gyro radius associated with the beam current, the Weibel-like instabilities[7] are stabilized and the electrons are then subject to the scattering, straggling, and blooming processes described herein.

III. THE MODEL OF ELECTRON ENERGY DEPOSITION

In the context of fast ignition, an analytic model[8,9] has recently been developed to address the energy deposition of energetic electrons in the dense core. Contrary to previous work,[14] this model rigorously treats the effects of the energy loss due to electron scattering and delineates the inextricable relationship of straggling and blooming with enhanced electron energy deposition. Specifically, the linear energy stopping power is given

$$\frac{dE}{dx} = < \cos\theta >^{-1} \frac{dE}{ds} \quad . \tag{3}$$

where dE/ds is plasma stopping power (continuous slowing down)

$$\frac{dE}{ds} = \frac{-2\pi r_0^2 m_0 c^2 n_i Z}{\beta^2}\left[\ln\left(\frac{(\gamma-1)\lambda_D}{2r_0\sqrt{2\gamma}}\right)^2 + 1 + \frac{1}{8}\left(\frac{\gamma-1}{\gamma}\right)^2 - \left(\frac{2\gamma-1}{\gamma}\right)\ln 2 + \ln\left(\frac{1.123\beta}{\sqrt{2kT_e/m_0c^2}}\right)^2\right] \tag{4}$$

taken from Ref. 8, and

$$< \cos\theta >= \exp\left(- \int_{E_0}^{E} \kappa_1\left(E'\right)\left(\frac{dE'}{ds}\right)^{-1} dE' \right). \tag{5}$$

The effects of the scattering are manifested by the macroscopic transport cross sections of various orders (ℓ) which are all a function of the energy loss,

$$\kappa_\ell\left(E\right) = n_i \int \left(\frac{d\sigma}{d\Omega}\right)[1 - P_\ell(\cos\,\theta)]d\Omega \ . \tag{6}$$

In particular, when ℓ=1,

$$\kappa_1(E) = 4\pi n_i \left(\frac{r_0}{\gamma\beta^2}\right)^2 \left[Z^2 \ln\Lambda^{ei} + \frac{4(\gamma+1)^2}{\left(2^{\sqrt{(\gamma+1)/2}}\right)^4} Z \ln\Lambda^{ee} \right], \tag{7}$$

which relates to the slowing down cross section and characterizes the loss of directed velocity (momentum) in the scattering [11]; and when ℓ=2,

$$\kappa_2(E) = 12\pi n_i \left(\frac{r_0}{\gamma\beta^2}\right)^2 \left[Z^2\left(\ln\Lambda^{ei} - \frac{1}{2}\right) + \frac{4(\gamma+1)^2}{\left(2^{\sqrt{(\gamma+1)/2}}\right)^4} Z\left(\ln\Lambda^{ee} - \frac{1}{2}\right) \right], \tag{8}$$

which relates to the deflection cross section and represents mean-square increment in the transverse electron velocity during the scattering process.[11] From Eq. (3), *dE/dx* is effectively enhanced over *dE/ds* due to the effects of the scattering (<cosθ> ≤ 1).

Furthermore, in our calculations, the longitudinal straggling is

$$\Sigma_R(E) = \sqrt{\langle x^2\rangle - \langle x\rangle^2} \ , \tag{9}$$

and the beam blooming is

$$\Sigma_B(E) = \sqrt{\langle y^2\rangle} \ , \tag{10}$$

(because of azimuthally symmetry, one has <y> = <z> = 0). Both Σ_R(E) and Σ_B(E) are calculated by evaluating basic moments required for the calculation of the longitudinal and lateral distributions:

$$\langle x\rangle = \int_{E_0}^{E} \langle P_1(\cos\theta)\rangle \left(\frac{dE'}{ds}\right)^{-1} dE' ; \tag{11}$$

$$\langle x^2\rangle = \frac{2}{3}\int_{E_0}^{E} \langle P_1(\cos\theta)\rangle \left(\frac{dE'}{ds}\right)^{-1} \left(\int_{E_0}^{E'} \frac{1 + 2\langle P_2(\cos\theta)\rangle}{\langle P_1(\cos\theta)\rangle} \left(\frac{dE''}{ds}\right)^{-1} dE'' \right) dE' ; \tag{12}$$

and

$$\langle y^2\rangle = \langle z^2\rangle = \frac{2}{3}\int_{E_0}^{E} \langle P_1(\cos\theta)\rangle \left(\frac{dE'}{ds}\right)^{-1} \left(\int_{E_0}^{E'} \frac{1 - \langle P_2(\cos\theta)\rangle}{\langle P_1(\cos\theta)\rangle} \left(\frac{dE''}{ds}\right)^{-1} dE'' \right) dE' \ , \tag{13}$$

where

$$\langle P_\ell(\cos\theta)\rangle = \exp\left\{ - \int_{E_0}^{E} \kappa_\ell(E') \left(\frac{dE'}{ds}\right)^{-1} dE' \right\} . \tag{14}$$

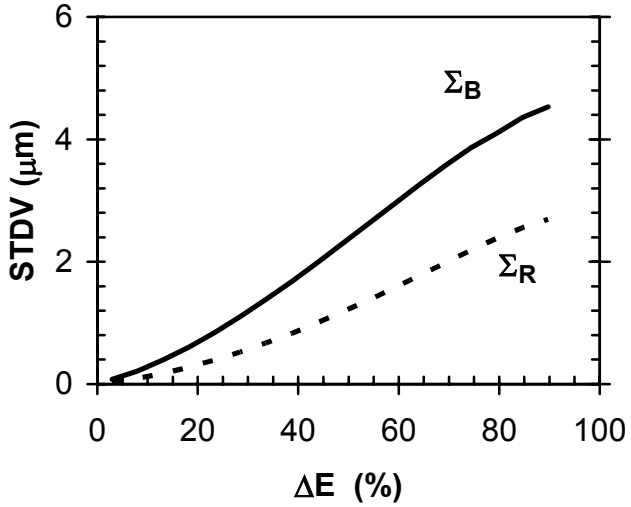

FIG. 7. The calculated range straggling $\Sigma_R(E)$ and beam blooming $\Sigma_B(E)$ as a function of electron residual energy for 1-MeV electrons in a DT plasma (ρ=300/cm^3, T_e=5 keV).

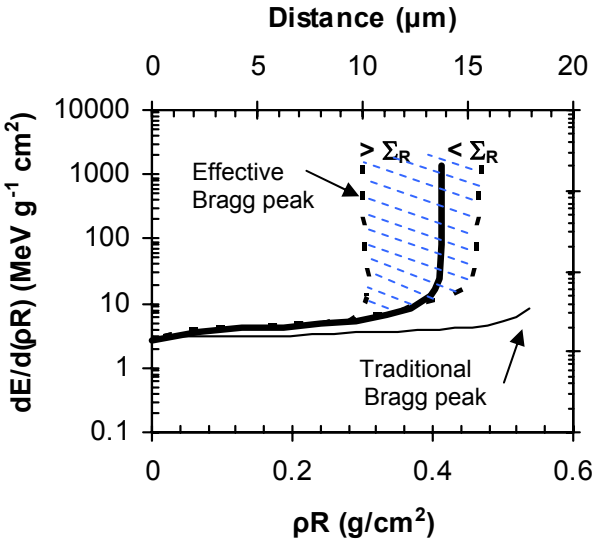

FIG. 8. The stopping power plotted as a function of the electron penetration for 1-MeV electrons in a DT plasma (ρ=300g/cm^3 and T_e=5 keV). The heavy solid line represents the mean energy loss, while the two dashed lines schematically indicate the straggling range over which energy is effectively spread. The thin line illustrates the continuous slowing-down approximation, [15-17] and is directly related to *R*, the total path length.

Figure 7 shows both $\Sigma_R(E)$ and $\Sigma_B(E)$ as a function of electron energy loss [$\Delta E=(E_0-E)/E_0$] for 1-MeV electrons in a DT plasma (ρ=300/cm^3, T_e=5 keV). As a consequence of the effects of energy loss upon the scattering, it is shown that the energy deposition, towards the end of the penetration, is transferred to an extended region about the mean penetration of 13.9 μm, specifically ~ ±3 μm longitudinally and ~ ±5 μm

laterally. Further illustrated in Fig. 8, the stopping power is now seen effectively enhanced in the extended region in which straggling and blooming are important. Such enhancement forms an effective "Bragg peak". In contrast, the traditional *electron* stopping Bragg peak[15,16] occurs at energies ~ 50 eV or less for Z=1, which results solely from the velocity match between the incident electron and plasma electrons and included no scattering at all.[17] The combined effects of blooming and straggling will result in an asymmetric energy deposition region about the mean penetration.

Figure 9 further shows the details of the energy deposition in a compressed target. Notable is the fact that little straggling or blooming occurs until the 1-MeV electrons have traversed a significant portion of the final penetration (~ 60%, corresponding to only ~ 40% energy loss). We can see that the assumption of uniform energy deposition, used in some previous calculations and also plotted in Fig. 9, has some approximate justification only for the first ~ 40% of the energy loss. For energy loss greater than 40%, both straggling and blooming expand linearly with the square root of the penetration, an effect associated with the enhanced energy loss of the effective Bragg peak. As a direct consequence of these multiple scattering effects, these results demonstrate the inextricably linkage between enhanced energy loss, straggling, and blooming.

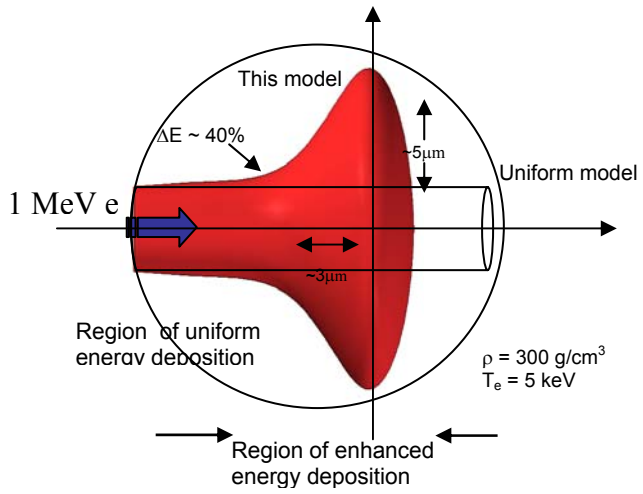

FIG. 9. Schematic illustration of the energy deposition profile for 1-MeV electrons in a DT plasma of 300g/cm^3 at 5 keV. After considering the mutual coupling between stopping, straggling and blooming, we find that the energy deposition towards the end of the penetration occurs in an extended, non-uniform region about the mean penetration of 13.8 μm, specifically~ ±5 μm laterally, and longitudinally > 3 μm in the backward direction and < 3 μm in the forward direction.

IV. DISCUSSIONS

To further delineate the basic features and applications of this model, the fundamental dependence of the scattering effects on plasma Z, density, temperature, and electron energy are discussed in this section. However, because of the non-linear

coupling of energy loss, straggling, and blooming, as is reflected in the complex integrands and limits in the double and triple integrals [for example, Eqs. (11) - (14)], there is no simple analytic reduction for these results. Thus, we will evaluate these effects and their dependences, albeit numerically, in the context of the fast ignition.

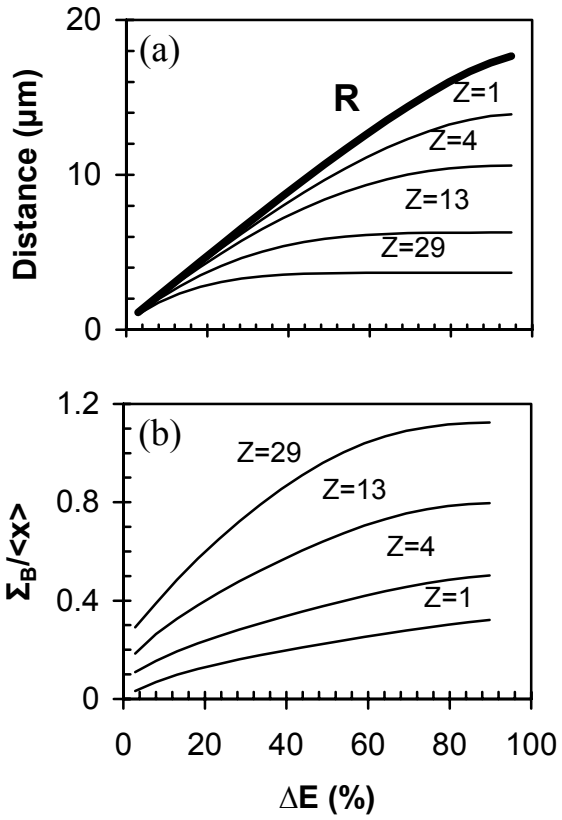

FIG. 10. The total path length (R), penetration ($<x>$) and blooming (Σ_B / $<x>$) are evaluated for interactions of 1 MeV electrons with DT, beryllium, aluminum and copper plasmas, assuming plasma T_e= 5 keV and n_e=7.2×10^{25} in every cases. For Cu plasma, bremsstrahlung loses are about 5%, and are ignored.

A. Dependence of scattering on plasma Z

The strong Z–dependence of scattering is directly reflected in the penetration, blooming and straggling. To explicitly illustrate this, both $<x>$ and Σ_B (Σ_B / $<x>$) are evaluated numerically for Z=1, 4, 13, and 29, and the results are plotted in Fig. 10. For facilitating the comparison, we have assumed that these plasmas all have the same electron density (n_e=7.2×10^{25} and T_e= 5 keV). With this assumption, the total path length ($R = \int_{E_0}^{\sim T_e} \left(dE/ds\right)^{-1} dE$),[18] which doesn't include at all the effects of scattering, should be identical for all these plasmas because energy loss to plasma electrons is the only mechanism for electron stopping. However, as shown in Fig. 10(a), including the effects of scattering significantly decreases the penetration. In particular, with increasing Z, the

penetration, but not the total path length, rapidly drops and blooming effects ($\Sigma_B/\langle x\rangle$) notably increase [Fig. 10(a) and 10(b)]. This strong Z-dependence results directly from the macroscopic transport cross sections, Eqs. (7) and (8), where the scattering scale as Z^2 and will play an overwhelmingly dominant role for higher Z plasmas.

B. Dependence of scattering on plasma density

As illustrated in Fig. 11, the scattering effects ($\Sigma_R/\langle x\rangle$ and $\Sigma_B/\langle x\rangle$) and $\rho\langle x\rangle$ are insensitive to the plasma density. This insensitivity results from the effective cancellation of the density in these calculations. (For example, $\rho \propto n_i$ while $\langle x\rangle \propto n_i^{-1}$. The slight increase in $\rho\langle x\rangle$ with density simply reflects the slight decrease in the Coulomb logarithm of the stopping power as the density increases). The significance of these results is that the overall effect of the scattering is solely determined by the areal density that these electron travel through. Consequently, the plasma density gradients, such as would occur towards the core region of an actual fast ignition experiment, will not impact the general scope or the final results of these calculations.

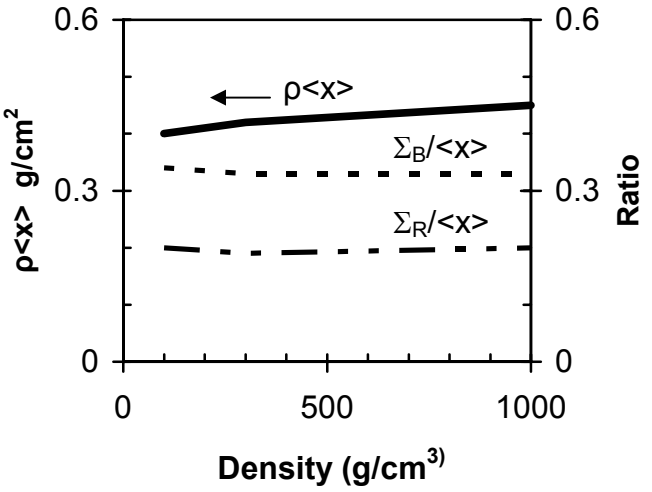

FIG.11. The scattering effects ($\Sigma_R/\langle x\rangle$ and $\Sigma_B/\langle x\rangle$) and the areal density ($\rho\langle x\rangle$) for 1 MeV electrons in DT plasmas, plotted as a function of the plasma density. The dependence of scattering are shown to be relative insensitive to the densities in this regime.

C. Dependence of scattering on plasma temperature

The temperature dependence is shown to be weak; As illustrated in Fig. 12, a factor of 10 reduction in temperature results in only a ~ 10% reduction in the penetration. This is because the projectile electrons are so energetic compared to the background plasmas that plasma temperature dependence is weak. However, as the initial electron energy decreases, the effect of scattering becomes more pronounced (this is similar to what is seen in the scattering of energetic electrons in metals[19]). For a given electron energy, scattering effects slightly decrease as the target plasma temperature decreases, *i.e.*

the path of an electron slightly straightens as the target plasma temperature drops. For example, when the target plasma temperature changes from 5.0 to 0.5 keV (ρ=300 g/cm^3), the ratio $R/\langle X_p \rangle$ is reduced by ~ 5% for 1-MeV electrons.

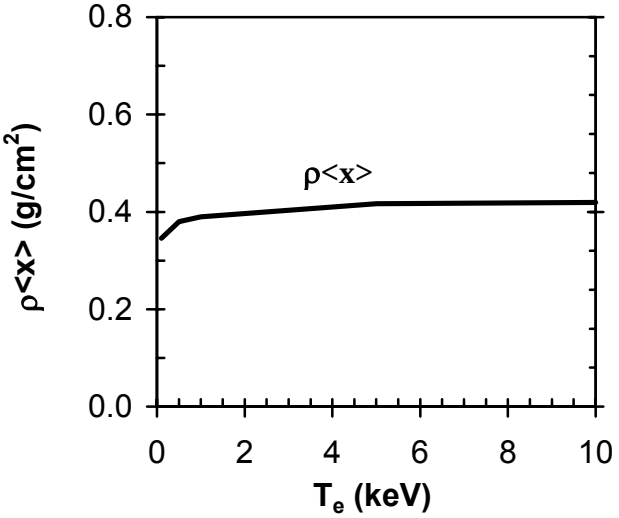

FIG. 12 The calculated penetration of 1-MeV electrons as a function of plasma temperature in a DT plasmas with ρ=300g/cm^3. It is seen that $\rho\langle x \rangle$ is relatively insensitive to plasma temperature.

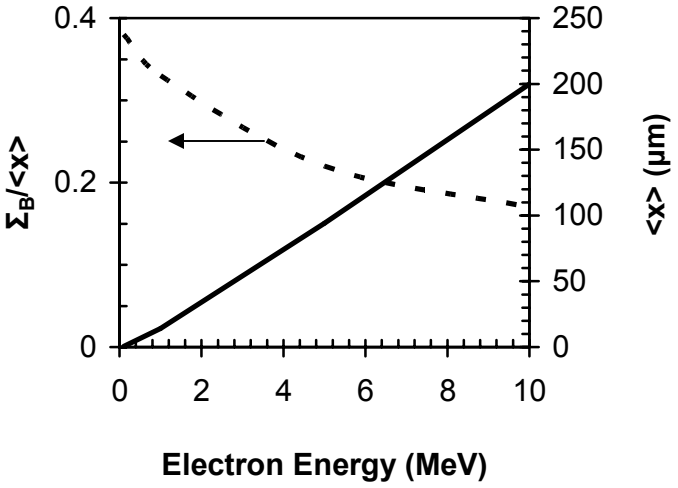

FIG. 13. Illustration of the enhancement of scattering effects ($\Sigma_R/\langle x \rangle$ and $\Sigma_B/\langle x \rangle$), as well as the electron penetration, as the electron energy decreases from 10 to 0.1 MeV in a DT plasma of 300g/cm^3 at 5 keV.

D. Dependence of scattering on electron energy

Finally, the dependence of scattering on projectile electron energy is explicitly illustrated in Fig. 13: while electrons with higher energy penetrate farther, the scattering effects ($\Sigma_R/\langle x\rangle$ and $\Sigma_B/\langle x\rangle$) are significantly enhanced as the electron energy decreases from 10 to 0.1 MeV. These effects are also important for the electron preheat problem,[20,21] even for regimes of lower energy and much lower density.

V. SUMMARY

In summary, we have analytically modeled the energy deposition of MeV electrons in dense plasmas in the context of ICF fast ignition. It is found that the effects of classical stopping and scattering dominate the electron transport and energy deposition in the region of dense plasmas. The calculations presented in this article rigorously treat the effects of the energy loss due to multiple electron scattering, as well as the effects of longitudinal straggling and transverse blooming, and their inextricable relationship with enhanced electron energy deposition. The penetration of 1-MeV electrons is reduced from 0.54 to 0.41 g/cm^2. In particular, it has been demonstrated that, while the initial penetration results in approximately uniform energy deposition, the latter penetration has mutual couplings of energy loss, straggling, and blooming that lead to an extended region of enhanced, non-uniform energy deposition. This model can be used for quantitatively assessing ignition requirements of fast ignition.

ACKNOWLEDGMENTS

This work was supported in part by U.S. Department of Energy Contract #DE-FG03-99SF21782, LLE subcontract #PO410025G, LLNL subcontract #B313975, and the Fusion Science Center for Extreme States of Matter and Fast Ignition Physics at University of Rochester.

[1] M. Tabak, J. Hammer, M. Glinsky W. L Kruer, S, C, Wilks, J. Woodworth, E. M. Campbell, M. D. Perry, and R. J. Mason, Phys. Plasmas **1**, 1626 (1994).
[2] S. Atzeni, Phys. Plasmas **6**, 3316 (1999).
[3] S. Atzeni and J. Meyer-Ter-Vehn, *The Physics of Inertial Fusion* (Clarendon, Oxford, 2004).
[4] A. Pukhov and J. Meyer-ter-Vehn, Phys. Rev. Lett. **76,** 3975 (1996).
[5] M. Honda, J. Meyer-ter-Vehn and A. Pukhov, Phys. Rev. Lett. **85,** 2128 (2000).
[6] L. Gremillet, G. Bonnaud, and F. Amiranoff, Phys. Plasmas **9,** 941 (2002).
[7] E. S. Weibel, Phys. Rev. Lett. **2**, 83 (1959).
[8] C. K. Li and R. D. Petrasso, Phys. Rev. **E. 70**, 067401 (2004).
[9] C. K. Li and R. D. Petrasso, "Stopping, Straggling and Blooming of Directed Energetic Electrons in Hydrogenic and Arbitrary-Z Plasmas", accepted and to be published in Phys. Rev. **E.** (2005).
[10] L. Spitzer, *Physics of Fully Ionized Gases* (Interscience, New York, 1962).
[11] B. Trubnikov, *Review of Plasma Physics* 1 (Consultants Bureau, New York, 1965).
[12] S. I. Braginskii, *Review of Plasma Physics* 1 (Consultants Bureau, New York, 1965).

[13] H. M. Milchberg, R. R. Freeman, S. Davey, and R. More, Phys. Rev. Lett. **61,** 2368 (1988).
[14] C. Deutsch, H. Furukawa, K. Mima and K. Nishihara, Phys. Rev. Lett. **77**, 2489 (1996). Erratum, Phys. Rev. Lett. **85**, 1140 (2000).
[15] R. D. Evans, *The Atomic Nucleus* (McGraw-Hill, new York, 1955).
[16] M. J. Berger and S. M. Seltzer, National Academy of Science – National Research Council Publication 1133 (1965); L. Pages, E. Bertel, H. Joffre and L. Sklavenitis, Atomic Data **4**, 1-127 (1972), and references therein.
[17] The traditional Bragg peak cannot be reflected in the "continuous slowing down calculations" since we integrate down to energy loses corresponding to 95% of the initial energy, which is well above this energy. This is of course in contrast to the *ion* Bragg peak, which occurs at energies of ~ 100 keV, and which is physically realizable in many circumstances and experiments.
[18] C. K. Li and R. D. Petrasso, Phys. Rev. Lett. **70**, 3059 (1993).
[19] K. H. Weber, Nucl. Instrum. Methods **25**, 261 (1964).
[20] M. D. Rosen, R. H. Price, E. M. Campbell, D. W. Phillion, K. G. Estabrook, B. F. Lasinski, and J. M. Auerbach, S. P. Obenschain, E. A. McLean, R. R. Whitlock, and B. H. Ripin, Phys. Rev. A **36**, 247 (1987).
[21] J. D. Lindl, *Inertial Confinement Fusion* (Springer, New York, 1998).